DESIGN OF MACHINES AND STRUCTURES

A Publication of the University of Miskolc

Volume 8, Number 2 (2018)

EDITORIAL BOARD

CONTENTS

SIMPLIFIED CAD MODEL OF HUMAN METACARPAL
FOR IMPLANTATION

PÉTER FICZERE–PÉTER BOGYA–ESZTER HORVÁTH–LÁSZLÓ LOVAS
Budapest University of Technology and Economics,
Department of Vehicle Elements and Vehicle-Structure Analysis
1111 Budapest, Sztoczek u. 2.
ficzere@kge.bme.hu

Abstract: Due to the increasing availability of additive manufacturing technologies, the need for individualized medical implants also increases. Among the development steps of this type of implant, image processing and CAD modeling have a huge influence on the usability of implants. The possibilities of CAD modeling using image processing methods are analyzed in our present work.

Keywords: CT scan, stl, CAD model, bones, Finite Element Analysis

1. INTRODUCTION

Due to the extremely fast development and cost reduction of additive manufacturing technologies, the so-called 3D printing methods generally used in the engineering industry for the production of prototypes are increasingly becoming available in all areas of life [1]. Thus, the need for utilization in medical science has been also emerged [2].

Bone replacement may be required for a number of surgical interventions due to their serious defect. Nowadays, typically, series-made implants are used, which are only made in a certain series of sizes. Optionally, the patient or doctor selects and implants with the most appropriate size.

However, in extreme cases due to the patient's anatomy or facial features, these series-manufactured implants are difficult to use or ineffective at all. Here comes the need to deviate from serial production and create unique implants.

These unique implants are more representative of the original bone geometries, and the design can optionally be modified to make the final implant appropriate in all respects [3].

Traditional implants are mainly made of biocompatible corrosion-resistant steel or titanium alloys. The mechanical properties of such bone substitutes can largely differ from human bone due to the material and geometric demands.

With the time, this results in damage of the bones connected to the implant, and lead to the loosening of the implant and finally it should be replaced.

From this it can be seen that the individual implants are not only necessary due to the nature of the defects, the additive manufacturing technologies also offer much more favorable mechanical property.

Thus, the implants of which material characteristics are close to the original bone can be manufactured. [4], [5] Therefore, the 3D model of these implants should be designed to be suitable for finite element analysis after modeling and based on the simulation result, the model can be modified, if there is too much different in the mechanical behavior compared to the original bone [6].

In most cases, we can only estimate the material properties of the original bone as they depend on age, health and type of bone. [7], [8]

2. Process

The design and manufacture of individual implants consists of several stages. This article deals with the creation and then the simplification of the 3D model of the reproductive bone, namely the implant design.

3. 3D MODELING

3.1. CT scan of the defect

The input information for 3D modeling is given in our case by a CT (Computed Tomography) scan.

The subject of the study is a high osteoporotic human metacarpale removed from one of the hands of an elderly lady. We can use DICOM files made by CT equipment of the examined bone to construct a 3-dimensional model.

Figure 1. Location of human metacarpale in the hand

These files can be displayed as grayscale layers, where each pixel stores the weakening value associated with a particular segment of the scanned object. These files

contain other data that refer to the patient, the distance of the layers, and the size of the objects on the pictures.

Most tissue types represent different weakening range. [9] Thus, after converting DICOM files to a picture file format, using image processing methods allow us to separate the examined tissue – in this case the bone – from its environment and to create a model.

3.2. Image processing in MATLAB

The image files from the CT recordings were processed using MATLAB, which is one of the most versatile software in engineering field. [10]

MATLAB is able to automatically load and process the image layers in accordance with code without any action. It is possible to run the program automatically because the images are derived from one record and their sizes are the same in pixels and the distance of each pixel – in the specified directions – is the same.

Their names have been also sorted and the distance between the layers is the same. This also means that in almost all cases, if you want to start processing a new CT record, the input parameters listed above have to be given in the program.

The program reads and processes the images file one by one in the right order. After reading, each image is stored as a 2-dimensional matrix, where each element of the matrix corresponds to one pixel. From here, the processing operations use these matrices.

The first step in processing is masking: removing parts with greater intensity around the bone. For this, a polygon is defined around the bone, which forms a mask and the intensity of the pixels outside the mask is reduced.
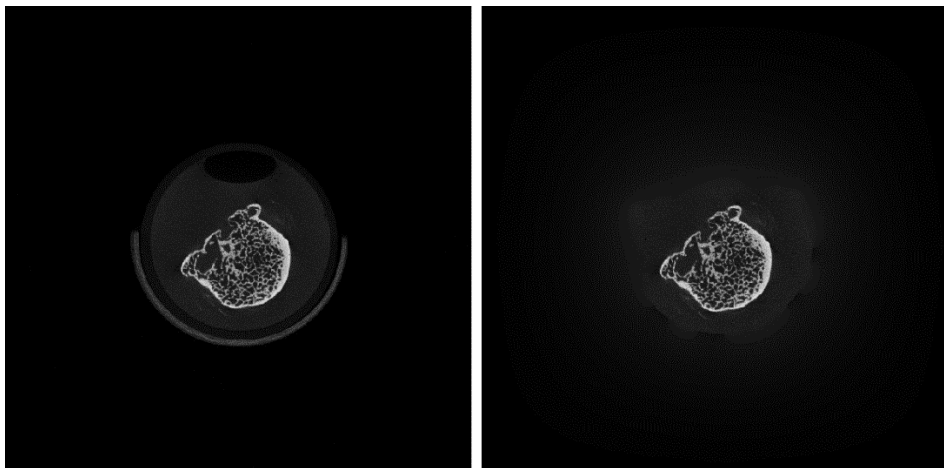
Figure 2. Original image on the left, after masking on the right

In the next step, the image was binarized, whereby the 2-dimensional matrix will contain only ones and zeroes, where the threshold is set according to the particular intensity limit for each pixel.

Many small spots can be seen on the left image of *Figure 3* right after binarization. These tiny spots are removed (right image) so the 3-dimensional model does not have any small floating particles in the bone model.

Figure 3. The image right after binarization (left), the image after elimination the small object (right)

Although the best approach of the original geometry is right image of *Figure 3*, the created model from these images could be difficult to produce even with the best 3D printers, and the finite-element simulations of this model would not be possible at all. [8], [11]

Thus, its strength properties could not be predetermined. Therefore, the next step is to simplify the inner part by filling the so-called holes, while retaining the outer geometry. The result of the 'filling' is shown on the left side of *Figure 4*.

Finally, the outer contour of the bone was modified to be smoother, the circumference of the bone slices is more uniform.
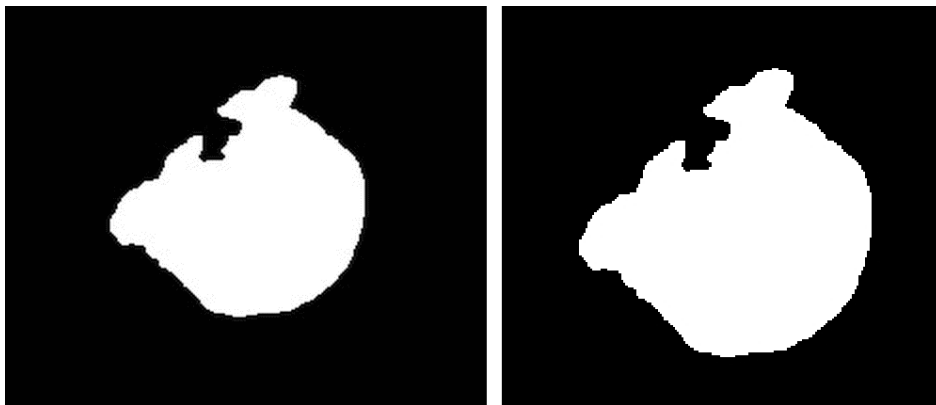
Figure 4. Image after the holes are filled (left), with the 'smoothed' circumference (right)

3.3. Preparation of surface model in MATLAB

The result of smoothing process can be seen on the right picture in *Figure 4*. The picture can be displayed as an image, but this is still a binary two-dimensional matrix.

The two-dimensional matrices resulting from the processing of all images are stacked together to form a three-dimensional matrix. In addition to the three-dimensional matrices, there are also three special vectors that define the normal distance between the layers of the matrix in the x, y, z directions from an arbitrarily selected base point.

After this, everything is done to make the surface model from bone. Another MATLAB function can generate a surface model from the loaded data as an output, which is an STL file.

The generated surface model is shown on the left picture of *Figure 5*.

4. MODEL TRANSFORMATION

4.1. Improvements in the model

The created model may still contain many errors in this form. This can be:

- slight angularity of the layered structure,
- floating objects separated from the bone, which have not been eliminated during image processing because of their larger size,
- protrusions (that are not belong to the original bone) resulting from the errors of image processing,
- surface openness,
- inclusions inside the bone.

These failures will be corrected.
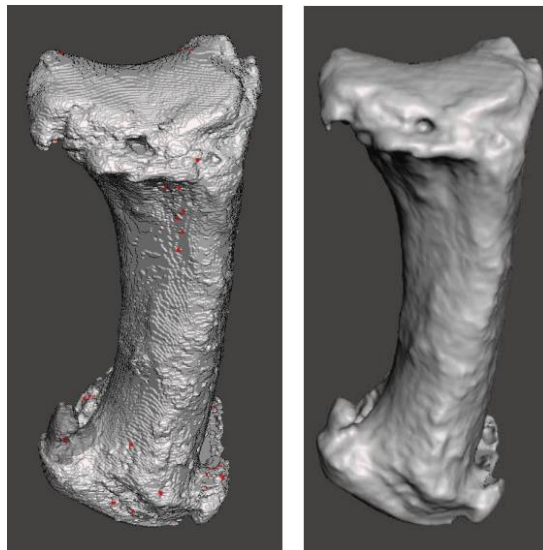
Figure 5. Original (left) and improved surface model (right)

4.2. Construction of solid model

In general, surface models are not suitable for finite element simulations, so they have to be converted to a solid model. The generated model is a solid model with triangular surface mesh corresponding to the mesh of the surface model.

This model could already be suitable for finite element modeling, but since the triangles that covers the surface are very small, the element size would be also very small in the finite element software.

Further, this would cause many calculations for the software, which requires a lot of time and computer resources. To avoid this, we simplify the model.

4.3. Simplification of the model

It is possible to simplify the model by cutting it at the appropriate spaces and replace the intersections with NURBS curve. Through the created curves, we perform a so-called swept extrusion. Thus, we re-create a part of the model that has no triangular surface [3].

However, the swept extrusion is not suitable to fork off in two or more directions. To eliminate this, the part of the model is simplified, and where this occurs the small surface triangles are merged and redefined and finally the swept extrusion method can be re-applied on the forks.

It is easier to perform a finite element analysis on this models with their much simpler surface geometry.
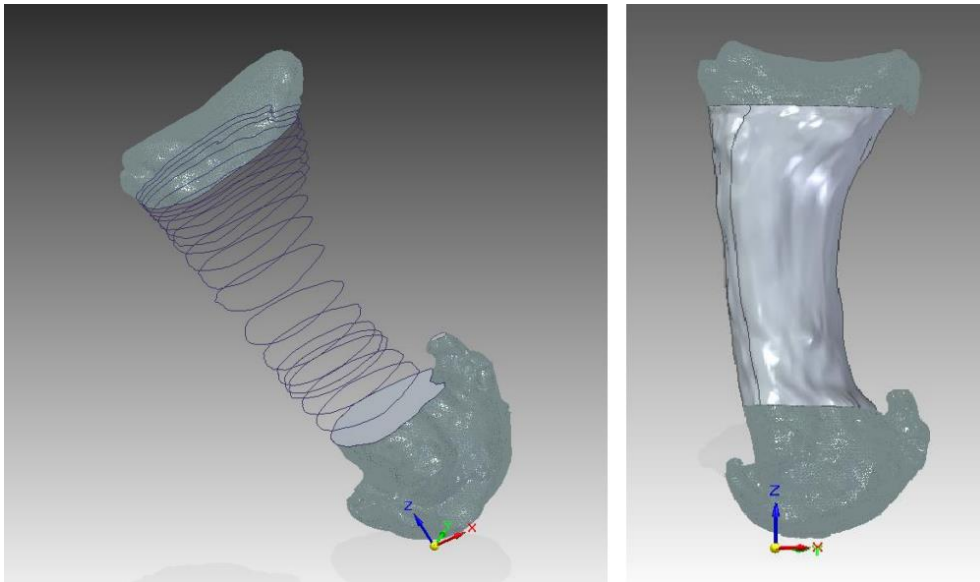
*Figure 6. The curves drawn one by one (left), the rebuilt model
by the curves (right)*

The geometry obtained after the simplification is virtually unchanged from the original geometry after the manufacturing, as it is shown in *Figure 7*. This means that the handling of the simplified geometry has improved significantly, while the loss of information during the simplifications (formal deviation from the original geometry) is almost neglible.

Figure 7. Original and simplified geometry after printing

5. SUMMARY

At an early stage in the design of a personalized bone replacement implant, image processing allows us to freely adjust the geometry before modeling, while retaining the outer contour. The reconstruction of solid model with NURBS curves can be a good solution to simplify it.

ACKNOWLEDGEMENT

REFERENCES

[1] Ficzere, P., Borbás, L., Török, Á. (2013). Economical Investigation Of Rapid Prototyping. *International Journal for Traffic and Transport Engineering*, 3 (3) pp. 344–350.

[2] Ficzere P., Borbás L. (2014). Gyors prototípus anyagok orvosi alkalmazásának lehetőségei, kérdései. In: Borbás Lajos (szerk.). *Korszerű anyagok és gyártástechnológiák alkalmazása a gyógyászatban*. Konferencia helye, ideje: Tatabánya, Magyarország, 2014. 05. 30–2014. 05. 31. Magyar Biomechanikai Társaság, p. 17.

[3] Győri M., Ficzere P. (2016). Increasing Role of Sections Caused by 3D Modelling. *Periodica Polytechnica-Transportation Engineering*, 44 (3), pp. 164–171.

[4] Popovics J., Manó S., Kiss R. M. (2018). Személyre szabott csontpótló implantátumok előállításának folyamata irodalomfeldolgozás alapján. *Biomechanika Hungarica*, XI. évfolyam, 1. szám.

[5] Ficzere P., Borbás L. (2018). Csont anyagtulajdonságainak megfelelő anyagmodellek előállítása additív gyártástechnológiákkal. *Biomechanica Hungarica*, 11, (2), p. 77–83.

[6] Ficzere P., Borbás L. (2017). Csontok anyagjellemzőinek közelítése a gyártástechnológiai paraméterek módosításával 3D nyomtatás esetén. *Biomechanica Hungarica*, 10 (2), p. 22.

[7] Reddy, M. V. K., Ganesh, B. K. C., Bharathi, K. C. K., ChittiBabu, P. (2016). Use of Finite Element Analysis to Predict Type of Bone Fractures and Fracture Risks in Femur due to Osteoporosis. *J Osteopor Phys Act*, 4:180. doi: 10.4172/2329- 9509.1000180

[8] Ficzere, P. (2018). Design questions of the individual medical implants. *Proceedings of the 4th International Interdisciplinary 3D Conference Engineering Section*, Pécs, Hungary, October 5–6, 2018, pp. 57–67.

[9] Mustra, M., Delac, K., Grgic, M. (2008). Overview of the DICOM Standard. *50th International Symposium ELMAR-2008*, 10–12 September 2008, Zadar, Croatia.

[10] Bogya P., Ficzere P., Horváth E., Lovas L. (2018). Csontokról készített CT felvételektől a CAD geometriáig. *GÉP*, LXIX. évfolyam, 4. szám, pp. 21–24.

[11] Győri, M., Ficzere, P. (2017). Use of Sections in the Engineering Practice. *Periodica Polytechnica-Transportation Engineering*, 45 (1), pp. 21–24.

USE OF NONLINEAR MATERIAL BEHAVIOR
WITH FEM-AIDED MATERIAL SELECTION

PAVEL FLORIAN–IVANA MAZÍNOVÁ–
MARTIN KRATOCHVÍL–FILIP HRDLIČKA
University of West Bohemia, Department of Machine Design
Univerzitni 8, 306 14 Pilsen
pflorian@kks.zcu.cz
mazini@kks.zcu.cz
kratochv@kks.zcu.cz
ficeriov@kks.zcu.cz

Abstract: This paper follows up the initiative to derive material indices and support material selection using finite element method. Material indices are a very useful tool helping with comparing different materials based on their properties performance in various applications. In this paper nonlinear material behaviour is introduced in this process demonstrated on a rubber seal application with self-contact.

Keywords: materials selection, FEM, nonlinear, material indices, Abaqus

1. INTRODUCTION

When creating a product material selection plays an essential role that significantly influences its properties. The methodology of materials selection described in [1] involves following steps. Firstly there are requirements on the product that can be broken down into four main groups: functions, constraints, objectives and finally free variables. The purpose of the product is defined by its function, e.g. to transmit force. Usually there are some boundaries that cannot be exceeded, such as total dimension or weight. These are expressed by constraints. When designing a product we also aim for some target or an objective. The product aims to be the best in terms of e.g. power output. Finally we are left with free variables that can be adapted to accomplish our objective and make the most of it.

In *Figure 1* this is summarized by the first row. The important step is to translate the entities in the first row into a measure that can be used for quantifying, comparing and ranking. In this case the measure is called a material index. Based on the value of the index we can sort the materials and determine how suitable they are for our product based on the given properties.

Below you can find a simple performance equation for mass of an oar loaded in bending [1]:

$$m = \left(\frac{4\pi S^* L^3}{3} \right)^{\frac{1}{2}} \cdot (L) \cdot \left(\frac{\rho}{E^{\frac{1}{2}}} \right) \tag{1}$$

The first bracket represents stiffness properties, the second term L stands for dimensional requirements and the last fraction represents the material index. The material index from the equation above is a typical example of indices presented in [1]. These indices were derived for very simple linear problems such a simple tension and bending. In our previous papers on this topic we involved finite element method in the process of material selection. This approach proved to be useful when dealing with more complicated problems involving different load cases and geometries [4, 6, 7]. This paper makes a step further and introduces how to take into account material nonlinearity.
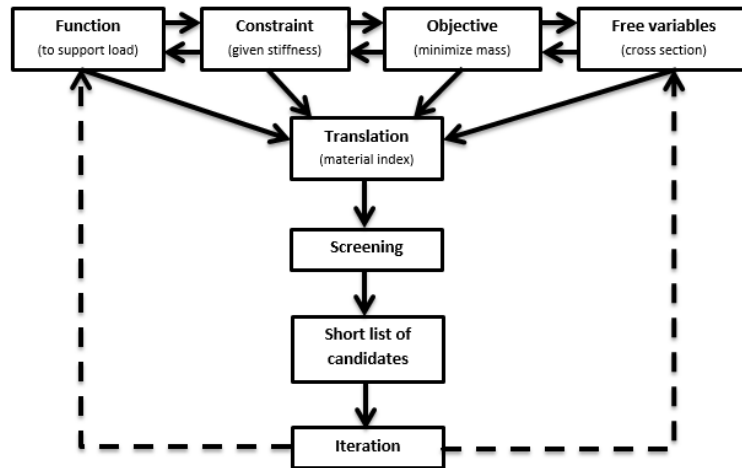
Figure 1. Materials selection process [4]

2. NEO-HOOKEAN NONLINEAR MODEL

The Neo-Hookean model is a rather simple nonlinear model suitable for hyperelastic materials that are similar in behaviour to rubber. This material model will be used further in the paper. Its strain energy potential is given by the following equation [3]:

$$U = C_{10}(\bar{I}_1 - 3) + \frac{1}{D_1}(J^{el} - 1)^2, \tag{2}$$

Where U stands for the strain energy per unit of volume; C10 and D1 are material parameters that are temperature-dependant. I1 is the first deviatoric strain invariant which is defined in the following way [3]:

$$\bar{I}_1 = \bar{\lambda}_1{}^2 + \bar{\lambda}_2{}^2 + \bar{\lambda}_3{}^2, \tag{3}$$

Deviatoric stretches are defined as [3]:

$$\bar{\lambda}_i = J^{-\frac{1}{3}}\lambda_i, \tag{4}$$

Where J is the total volume ratio; J^{el} is the elastic volume ratio and λ_i stands for the i-th principal stretch. Bulk modulus and initial shear modulus are given by [3]:

$$K_0 = \frac{2}{D_1}, \mu_0 = 2C_{10} \tag{5}$$

Figure 2 below shows a typical response of a Neo-Hookean material model as a stress-strain curve.
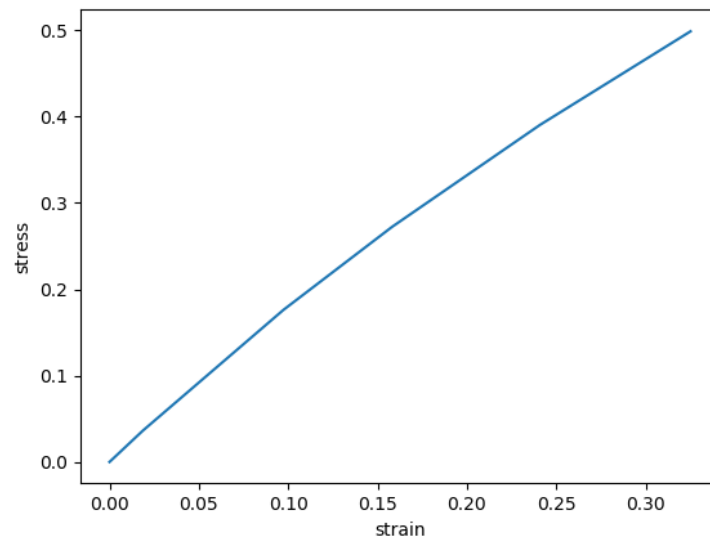
Figure 2. Stress-strain curve – Neo-Hookean

3. SELF-CONTACTING RUBBER SEAL EXAMPLE

The methodology will be demonstrated on a rubber seal example. The complexity of the chosen problem is due to occurrence of large deformations and self-contact of the rubber seal. Therefore, an explicit solver was chosen.

The rubber seal in a steel housing and an upper flange displayed as a line body can be seen in the *Figure 3* below.
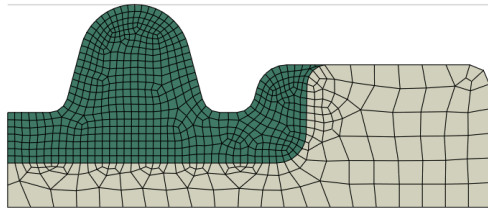
Figure 3. Rubber seal – undeformed state

An example of the rubber seal in the deformed state is in the *Figure 4.*
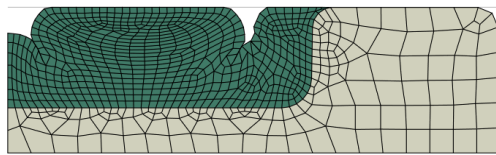
Figure 4. Rubber seal – deformed state

The analysis is setup in such way that the rigid upper flange has prescribed displacement in the vertical direction. Reaction force on the flange is measured. This represents the conditions during assembly. A range of parameters was used for both material model parameters C10 and D1. The whole design-of-experiment study consisted of 25 simulation runs. The finite element model is taken over from Abaqus documentation as is created using four-node plane strain elements CPE4R [3].

The results of the analysis as well as the fitted surface are displayed in *Figure 5* below. The horizontal axes represent D1 and C10 and the vertical axis stands for the reaction force.
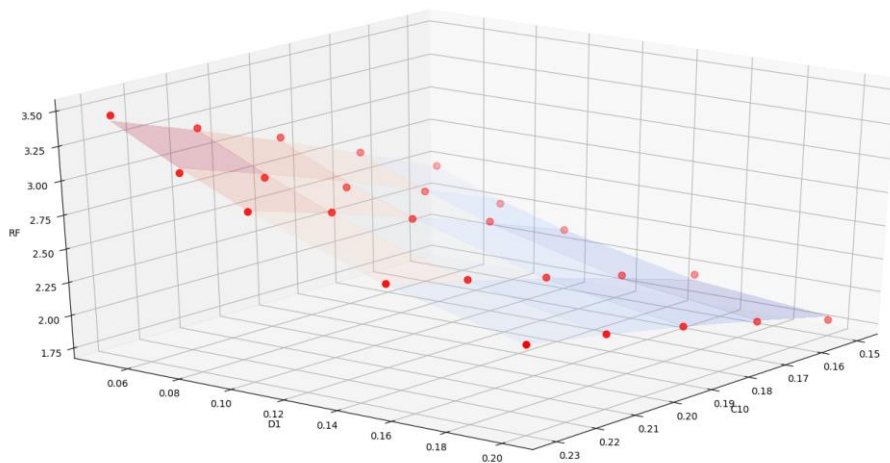
Figure 5. Results of DOE

The surface fitted to the simulation results is given by the following equation:

$$RF = k\frac{C_{10}^{0.669}}{D_1^{0.251}} \qquad (3)$$

This equation also represents the material index- the second row in *Figure 1*. If we want to make a step further to the Screening phase we need to derive the C10 and D1 constants for our candidate materials and use them in *Equation 3*. Then we can search for a maximum or a minimum value depending on if we need high or low assembly force.

4. CONCLUSION

The work presented in this paper continues the extension of material indices theory first introduced in [1] currently involving also the use of nonlinear materials. Parameters of a material model are subjected to a design-of-experiment simulation and a mathematical surface is fitted to the results. The equation of the surface contains the parameters of the model and determines the material index. We can search for the suitable materials based on their stress strain curve assuming that the material model is sophisticated enough to describe the true behaviour of the material correctly.

ACKNOWLEDGEMENT

REFERENCES

[1]   Ashby, M. F. (2011). *Material Selection in Mechanical Design*. Oxford: Butterworth-Heinemann.

[2]   CES EduPack 2013 Version 12.2.13. [DVD] Cambridge: Granta Design Limited, Granta Design Limited, 2013. 12, 2, 13, 0. [2] Kane, T. R., Levinson, D. A. (1985). *Dynamics: Theory and Applications*. New York, McGraw Hill, NY.

[3]   Smith, M. (2018). *ABAQUS/Standard User's Manual, Version 2018.* Providence: Simulia, RI.

[4]   Mazinova, I. et al. (2016). Support of Materials Selection Optimization using ANSYS. *Book of Proceedings ICMD 2016*. Zelezna Ruda, 7–9 September, 2016, Pilsen: University of West Bohemia in Pilsen, pp. 367–372.

[5]   Cui, X. et al. (2011). Design of Ligthweight multi-material automotive bodies using new material performance indices of thin walled beams for the material selection with crashworthiness consideration. *Material and Design*, 32, 2, pp. 815–821.

[6]   Florian, P. et al. (2017). FEM-Aided Material Selection Optimization. *MM Science Journal*, June, pp. 1855–1859.

[7]   Kratochvil M. et al. (2018). Materials Selection for Efficient Cross-section of Components. *EAN 2018. The 56th International Conference of Experimental stress analysis*, Harachov 5–7 June 2018.

BIODEGRADABLE TOOTHBRUSH

BARBARA KMETZ–BALÁZS MAGYAR–FERENC J. SZABÓ
University of Miskolc, Department of Machine and Product Design
3515 Miskolc-Egyetemváros
kmetzbarbara@gmail.com, m.balage12@hotmail.hu, machszf@uni-miskolc.hu

Abstract: During our third year we took part in an international project called Heibus project (https://www.linkedin.com/company/heibus-project). We got a topic according to which we had to work. This topic was biodegradable products. The next article is about these products and about how these products are developed. If you are in the habit of reading what supermarkets print on their plastic bags, you may have noticed a lot of eco-friendly statements appearing over the last few years. We followed this idea through our project as we designed and developed, eco-friendly products, as alternative to disposable polymeric products, that have a high impact on nature. We tried to reduce the environmental footprint through the development of new and biodegradable plastic products.

Keywords: biodegradable, polymer, toothbrush, 3D printing, FEM

1. BRAINSTORMING

For this matter we had to consider all the different fields where people use too much non-biodegradable items.

As we looked at all the different fields, which was not easy considering humans have a way of producing too much unnecessary products that can become trash over time.

One of the most effective ways of collecting ideas is brainstorming. It is a form of collecting new ideas, everything that comes to one's mind. There are no bad ideas in this stage of the gathering. We just wrote down everything that was considered useable for us. We looked at separate areas.

The first area was the Medical field. We could see many opportunities here though this is a very difficult matter to work with. We could list stitches, prosthetics, plasters, metal plates, arch supporters and spine corsets as interesting products to work with.

The second area we looked into was sports and games. We could think of mouthguard, safety garment, inflatable toys, wheels, plastic bottles and fishing tools to consider. This area looked more realistic for us.

Our third area was gardening, because as we were going through some books, we realized that many gardening techniques include leaving rubbish behind. So, we were thinking what if we can replace those items that accidently stay in the soil with biodegradable ones. This led us to think about watering tubes, watering cans, chairs, tables and different containers like underground containers.

The forth fields was full of opportunities. We looked at bathroom accessories and we discovered that tons of trash is piled up from almost every product found in bathrooms. Toothbrush, comb, razor, shampoo bottles was just some of the things we have found we could replace.

Kitchen tools were something many companies were already dealing with, including the Andaltec which is a non-governmental organization, so even though we found many things to works with like fork, knife, spoon, pet bottles, caps, plastic glasses, six packs, food containers and even egg holders we did not really see big opportunities here as these products are already being replaced.

We found random everyday tools we came across with, like plastic phone cases, cables, distributors, eye/sun glasses and their cases, keychains, ID folders and umbrellas.

Stationery products were also something to take into consideration. We could meet with plastic pens, highlighters, computer mice, plastic folders, keyboards and fans, but these items are used for a considerably long time, so these were eventually out of the question.

Other product we have found were traffic navigating tools, night time lamps, lamp shells. One really interesting idea was to replace festival grounds. Every summer when festivals come, there is a huge amount of rubbish after the events, but what if we could change some of the rubbish into biodegradable ones. Those paths they use against mud and rain are often made from plastic that cannot degrade, but if we replace those we could save some valuable amount. We only need those during the warm seasons, so it would be great considering the time of the degradation.

Last, but not least, we looked at our beloved little pets. We could also find many items that are replaced almost every year or so, like toys, plates, litter strays and poop collectors.

Other really great idea was to make biodegradable diapers since they are used so often (children, adults) and there is a great amount of trash from them, but as we search the market we discovered that these are already being made in several countries, so we could not follow this path either.

These were our first ideas we gathered and then we reduced them. *Figure 1* illustrates these possibilities.
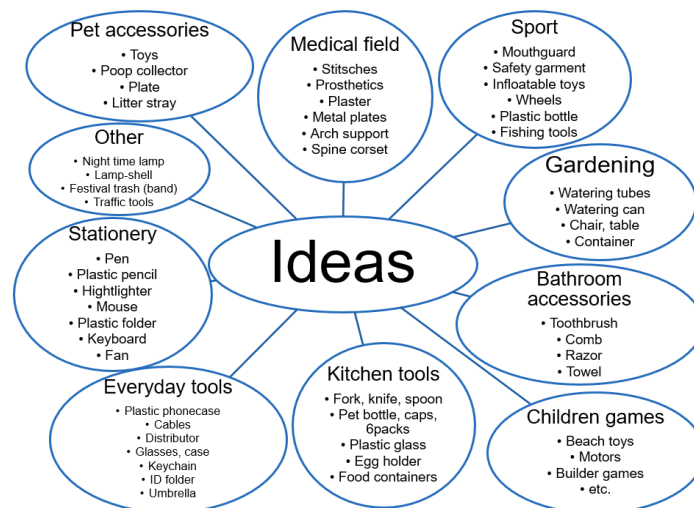
Figure 1. Brainstorming

2. CONSIDERED PRODUCT POSSIBILITIES

After long consideration we settled with bathroom accessories because we felt that this is a great field to work with. We collected all the tools we could imagine manufacturing from biodegradable polymer. We came across the next things:

- toothbrush
- toothpaste container
- floss container
- razor
- band aid
- cup
- comb
- shower cap
- shampoo bottle
- little traveling bottles

After taking all to consideration we decided to go on with designing a toothbrush. This seemed like the best option looking at environmental effects, designing, manufacturing and marketing.

Other products like combs would have had problem with designing and also manufacturing, beside they are not thrown away soon enough to make them out of biodegradable materials.

Band aids are a good idea, but we would have some problems with the sticking part and also the design cannot really change from the basics.

3. MARKET RESEARCH

Bogobrush is a biodegradable bamboo toothbrush. It has a simple, clean design and great colour choices. The bamboo colour is combined with turquoise, white and fresh green. These colours complete the design making the feeling of the toothbrush even more natural. Not only the handle is coloured but the brush too.

Figure 2. Market research I

We can see a closable toothbrush in *Figure 2*. It can be practical when traveling or if we are lack of place. The design does not look so nice and also the ergonomic aspect is not really great. The handle cannot be too comfortable. The green toothbrush is a concept design. It illustrates how they want to wash the teeth from every side. We are not sure about the function's potential as this one is just a concept.

We also found a closable toothbrush with a replacable head. This in *Figure 3* is closer to our thinking but the design and closability is still poor here. Next to it, there is a really practical toothbrush with a closing part. It is quite simple, but the texture is nice and the plus function that you can put it on the wall, makes the toothbrush one to look at.

Figure 3. Market research II

In *Figure 4* we can see some toothbrush concept sketches and a new concept next to them. This considerably big toothbrush has a unique function that has never been seen before. It works like a roly-poly toy as it has weight placed in the bottom, so it is always standing.

Figure 4. Market research III

Our other competition can be seen in *Figure 5*. Although it is bio, it looks quite casual, with nothing special or mentionable. It has the wood like texture and that is

all we can say about this product. Beside it, we can find a toothbrush with toothpaste in the bottom. The concept is that you can turn the bottom and as a result the toothpaste goes up to the top and you can brush your teeth, but this concept never made it to the stores because of the many difficulties, which appeared during testing.

Figure 5. Market research IV

4. CRITERIA SYSTEM

Our product is dedicated to all the people. It is an everyday common product so we cannot define one type or group of people, because everyone can use it.

Our original product was designed for adults, but since it has a replaceable head, we are planning to design one head for children as well with smaller brush and head.

Environment of our toothbrush:
We are designing it to any kind of environment where people are acceptant about it. We do not want to make a luxury product that only rich people can buy, we rather want to aim at larger layers of people, as a result our price should be reasonable.

Selected functions:
  – toothbrush
  – replaceable head
  – biodegradable material
    (further innovations: razor head, brush for braces, children brush head)

5. SKETCHES, DIFFERENT CONCEPTS

We came up with several different concepts during our project. These sketches were drawn on paper, so we scanned everything. In *Figure 6* our thinking can be followed.
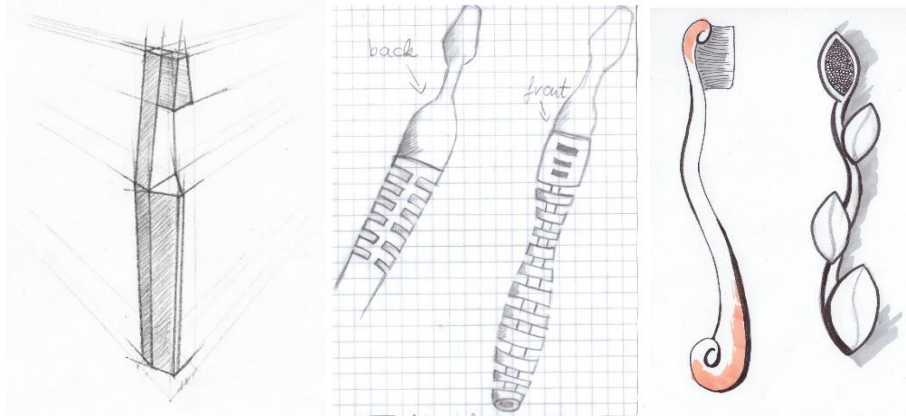
Figure 6. Hand drawn sketches

5.1. Searching 3D designs

We wanted to know how exactly 3D printed products are made and designed, so we looked up some 3D printed designs as inspiration to our designs. We came across quite a few of them, used in many fields. From printed prosthetics to toys, casts, statues and so on.

As this area (3D printing) is a considerably new field comparing to steel works or pottery, we tried to look at the aspects that makes this technique unique and different from the others. Finally, the big realization was that 3D printing methods can use less material with only printing the structure of the products. Once we set our minds on this concept it was the path to go on. In *Figure 7* it can be seen what we were referring to earlier.
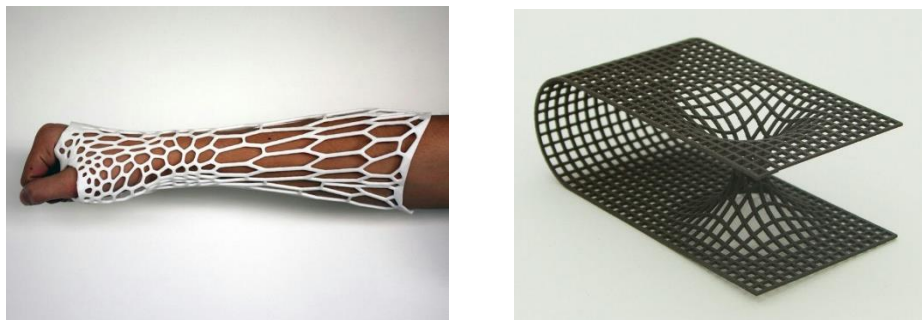
Figure 7. "Gap" designs

5.2. The "gap" design-Solid Edge models

As we were going through the designs, it was clear that it must be a simple one, because the injection part can only work with two sided designs, so we cannot put design all around the handle but only from two sides. This way it is possible to print

the design and also possible to inject it. After we considered the cut-out part's design we started to work on the 3D model and design.

Figure 8. Solid Edge design

5.3. Final design

The original design was suited for 3D printing, but it would have many difficulties with the manufacturing using injection, so we had to change the design to a simpler one.

Figure 9 shows how the printable and injectable model looks like.
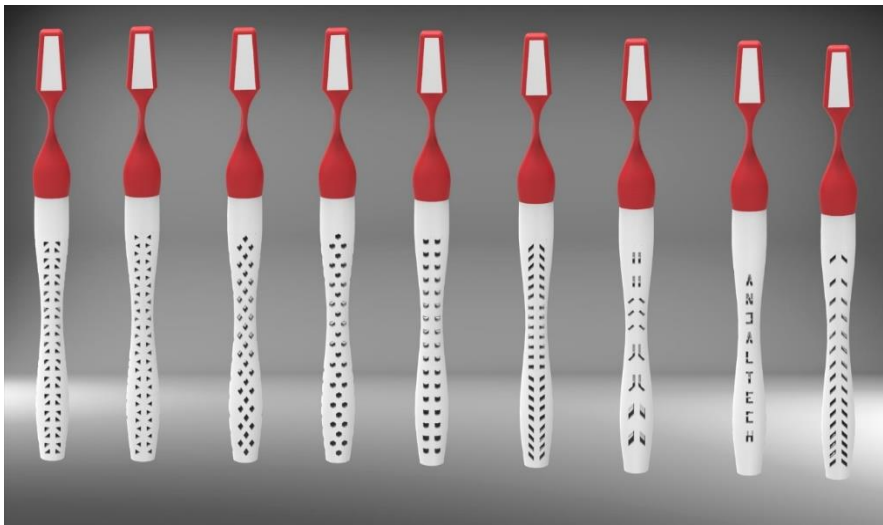
Figure 9. Solid Edge desings

6. FINITE ELEMENT METHOD

We ran a finite element method analysis on our product, so we could measure its mechanical attributes and deformations. We ran three different kind of analysis with different forces and fixed supports.
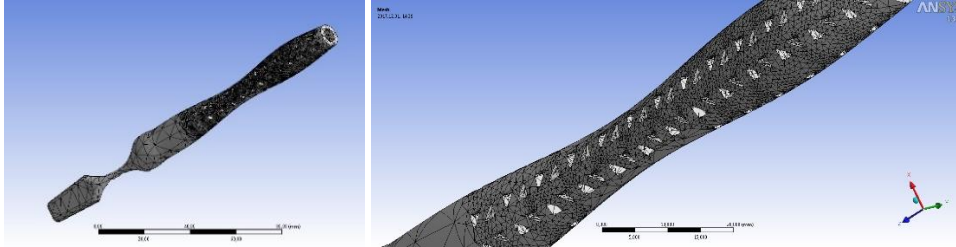
Figure 10. FEM mess

For our first analysis we had to import our item into the Ansys program, which we used for the analysis. The mesh of the product was quite complex, so it took some time to import and to make it. We added the pictures of our progress all through the way. In the first case we put a fixed support on the end of the handle and we put a 10 N force on the head. The corners showed the largest deformation, but even that was not dangerous to consider it.
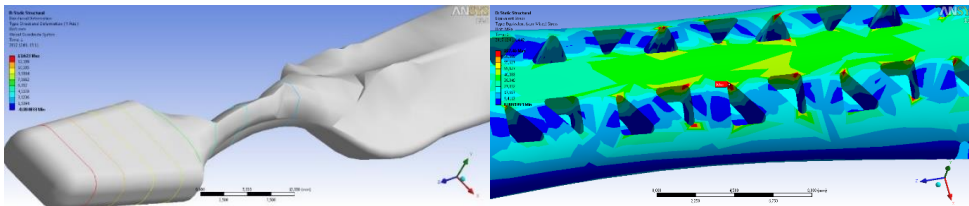
Figure 11. FEM I

For the second simulation we changed it up and put the fixed support on the head. We also put 10 N force on the body of the toothbrush. As it was expected, the toothbrush bended, but it was also eligible to work with.
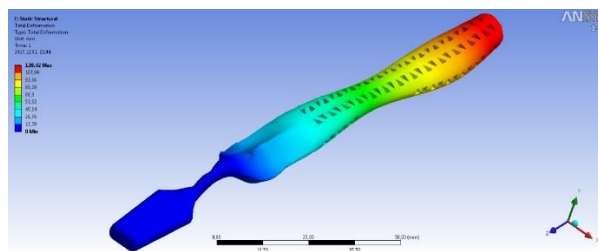
Figure 12. FEM II

For the third simulation we changed it up and put the fixed support on the head. We also put 10 N force on the body of the toothbrush. As it was also expected in this case, the neck gets the most stress from the deformation. We analysed the results and we found them suitable for our product, so the manufacturing process could continue.
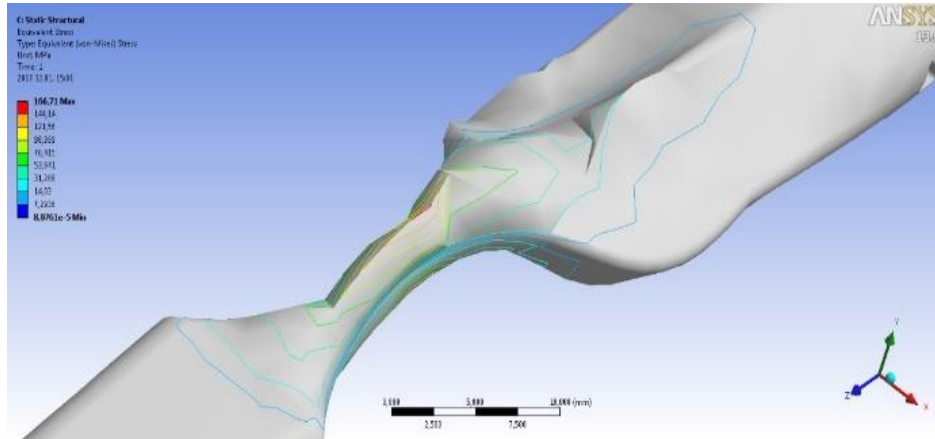
Figure 13. FEM III

7. PROTOTYPE

The "gap" design prototype:

We printed our prototype in the laboratory of the University of Miskolc in the Institute of Machine and Product Design. In a few days we could hold our prototype in our hands. It was printed with a one extruder printing machine, in laying down position. It took 3 hours and 42 minutes to print the toothbrush. The prototype is made out of our chosen material, biodegradable polyactic acid, PLA. It weighs 13 grams.

Figure 14. First prototype, other printed concepts

7.1. Additional ideas, future ideas

Other ideas were replaceable heads with different functions. We can design a razor head and use the handle for that razor head also. We could make a kid's toothbrush head since they need a smaller head and brush. We can also make a special brush for braces as an additional plus function. These are some future ideas to work with.

If there will be some different heads to the handle it will probably need a special stand for it and for the heads. The concepts in *Figure 15* show these possibilities.

Figure 15. Other accessories

7.2. Plus design idea

As an additional idea a special shaped toothbrush was also designed. This one has a unique structure, but its manufacturing is a different story. The printing process can work with multiple head printer, but the injection process is not possible at the moment for this design. It is noticeable that the white concept refers to teeth if we look up closely and we have a little imagination.
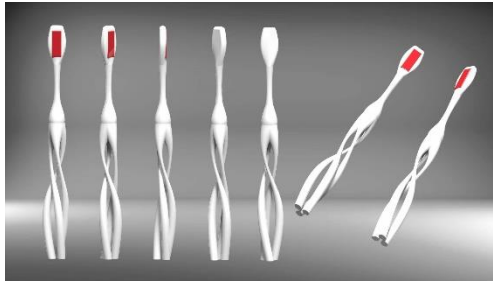
Figure 16. Tooth-like concept

8. ECOLOGICAL FOOTPRINT, LIFECYCLE
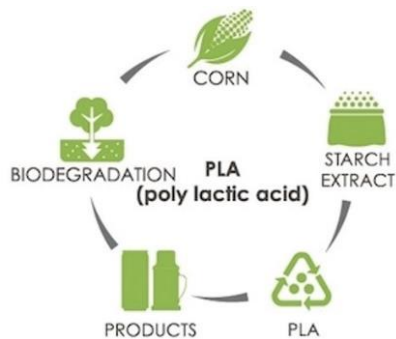
Figure 17. Lifecycle

It can be seen in *Figure 17* that opposite to the usually used plastic and nylon it can be composed. The plastic and nylon that make up the handle and bristles of your toothbrush both come from petroleum, a non-renewable resource with a long list of negative environmental impacts. Manufacturing nylon not only creates <u>nitrous oxide</u>, a greenhouse gas 310 times more potent than carbon dioxide, but it is an energy and water intensive process that results in runoff. Although it is difficult to get away from the nylon bristles, alternatives do exist. (from internet statistics-https://www.huffingtonpost.com/rosaly-byrd/the-environmental-footpri_b_5699007.html)

These sentences prove that toothbrush makes a valuable argument when talking about replacing an item with biodegradable polymer.

REFERENCES

[1]   Sin, L. T., Rahmat A. R., Rahman W. A. W. A. (2012). *Polylactic Acid. PLA Biopolymer Technology and Applications*. Elsevier.
[2]   Nofar, M., Park, C. B. (2017). *Polylactide Foams*. Elsevier.
[3]   Ebnesajjad, S. (2012). *Handbook of biopolymers and biodegradable plastics*. Elsevier.

NEW STABLE METHOD TO SOLVE HEAT CONDUCTION PROBLEMS IN EXTREMELY LARGE SYSTEMS

ENDRE KOVÁCS[1]–ANDRÁS GILICZ
[1]University of Miskolc, Department of Physics,
3515 Miskolc-Egyetemváros
fizendre@uni-miskolc.hu

Abstract: We present a new explicit and stable numerical algorithm to solve the homogeneous heat equation. We illustrate the performance of the new method in the cases of two 2D systems with highly inhomogeneous random parameters. Spatial discretization of these problems results in huge and stiff ordinary differential equation systems, which can be solved by our novel method faster than by explicit or the commonly used implicit methods.

Keywords: *heat transfer, heat conduction, numerical simulation, stiff equations*

1. Introduction and the studied problem

Experimental and numerical investigation of heat transfer in large-scale systems like chimneys of power plants [1], heat exchangers [2] and buildings [3] is a common problem for mechanical and heat engineers [4, 5]. In this paper we focus on only one of the mechanisms of heat transfer, the simplest Fourier-type heat conduction, but we hope that our results can be extended to heat transfer by radiation or even by convection.

Heat conduction phenomena are described by the heat equation, which is a second-order parabolic partial differential equation (PDE). Its homogeneous form is the following:

$$\frac{\partial T}{\partial t} = \alpha \Delta T \, ,$$

where $\alpha = \dfrac{k}{c\rho}$ is the thermal diffusivity, k, c, and ρ is the heat conductivity, specific heat and (mass) density, respectively. The phrase 'homogeneous' does not mean that the medium is physically homogeneous (i.e. α is constant), but, instead, that we do not deal with heat source terms, so in this paper we examine only transient processes.

Most PDEs for real-life problems cannot be solved analytically. The process of numerical solution usually begins with the discretization of the space variables (there are few exceptions, for example Rothe's method). One has to divide the whole spatial domain into (small) blocks, during which (in case of the heat equation) one have to calculate two quantities for each block. The first one is the heat capacity C of the block:

$$C = c \cdot m = c\rho V \left[\frac{J}{K} \right],$$

where m is the mass, V is the volume of the block. Now one can obtain the (thermal) energy of a cell j as $C_j \cdot T_j$, where T_j is the average temperature of the block. The second quantity is the heat/thermal conductance U, which can be approximated as

$$U_{ij} \approx k \frac{A_{ij}}{d_{ij}} \left[\frac{W}{K} \right],$$

where A_{ij} is the surface area between the two blocks i and j, while d_{ij} is the distance between the centres of the blocks. As we explained in our paper about analogies [6], quantities C and U are analogous to capacitance C and conductance (reciprocal resistance) $G = 1/R$ in case of electrical RC circuits where – of course – the electric charge is the flowing quantity.

After spatial discretization according to the usual central formula for the second derivatives [7]

$$\frac{\partial^2}{\partial x^2} f(x_i, t_j) \approx \frac{f(x_{i+1}, t_j) - 2f(x_i, t_j) + f(x_{i-1}, t_j)}{(\Delta x)^2},$$

we obtain an ODE system which gives the time derivative of each temperature:

$$\frac{dT_i}{dt} = \sum_{j=neigh} \frac{U_{ij}}{C_i} \left(T_j - T_i \right),$$

where the summation is going over the neighbours of the block. In order to help the reader to visualize, we present the arrangement of the variables in *Figure 1* for a 2D system of 4 blocks.
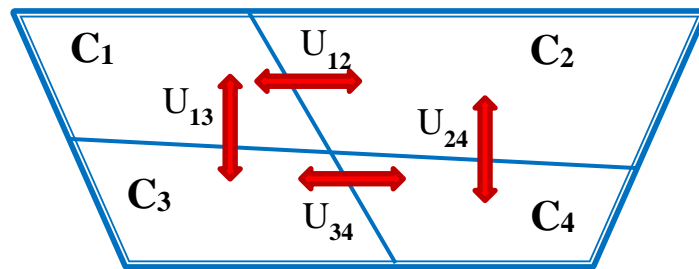
Figure 1. Notations in the case of four blocks. The outer thicker line represents thermal isolation. We emphasize that the shape and arrangement of the blocks are not necessarily regular

The ODE system in a matrix form for this small system:

$$\frac{d\vec{T}}{dt} = \begin{pmatrix} -\dfrac{U_{12}}{C_1} - \dfrac{U_{13}}{C_1} & \dfrac{U_{12}}{C_1} & \dfrac{U_{13}}{C_1} & 0 \\[2ex] \dfrac{U_{12}}{C_2} & -\dfrac{U_{13}}{C_2} - \dfrac{U_{24}}{C_2} & 0 & \dfrac{U_{24}}{C_2} \\[2ex] \dfrac{U_{13}}{C_3} & 0 & -\dfrac{U_{13}}{C_3} - \dfrac{U_{34}}{C_3} & \dfrac{U_{34}}{C_3} \\[2ex] 0 & \dfrac{U_{24}}{C_4} & \dfrac{U_{34}}{C_4} & -\dfrac{U_{24}}{C_4} - \dfrac{U_{34}}{C_4} \end{pmatrix} \vec{T}$$

One can see that the size of the matrix grows quadratically with the number of blocks, thus the number of elements of the matrix is inversely proportional with the 4th power of the diameter of the blocks (for a fixed system) and with the 6th power of the diameter in 3D. The absolute value of the matrix elements depends not only on the size (volume and surface) of the blocks but on the physical properties of the material like the specific heat and the thermal diffusivity as well. Since these parameters can largely vary from point to point, the magnitude of the matrix elements and therefore the eigenvalues can have a range of several orders of magnitude, which means it can be a severely stiff system.

Stiffness implies that conventional explicit methods are inappropriate because of unacceptably small timesteps. All available explicit integrators (with the possible exception of the Runge–Kutta–Chebyshev and the Alternating Direction methods) have a relatively small linear stability domain in the complex left half-plane [9, 10, 11]. This is the reason why they require unrealistically small step sizes for integrating stiff problems and they are rarely used in the industry. On the other hand, implicit methods require the solution of (usually nonlinear) algebraic equation systems at each time-step, moreover, it is not trivial to parallelize them. So when one has to quickly obtain an approximate result for a huge and stiff system, conventional methods provide no convenient solution. If the error tolerance is increased to enhance speed, explicit methods will diverge, while implicit ones still has to handle the huge matrices. Our task is to elaborate and new and easily parallelizable numerical algorithms and methods to solve these systems.

2. THE PROPOSED METHOD

We suggest the following simple formula to obtain the values of *T* at the end of the timestep using the values of *T* only at the beginning of the timestep:

$$T_i(t+h) = T_i(t) \cdot e^{-\frac{h}{\tau_i}} + \frac{\sum\limits_{j=neigh} U_{ij} \cdot T_j(t)}{\sum\limits_{j=neigh} U_{ij}} \cdot \left(1 - e^{-\frac{h}{\tau_i}}\right) \tag{1}$$

where $\tau_i = \dfrac{C_i}{\sum\limits_{j=neigh} U_j}$ is the characteristic time of the block. With this formula we try

to imitate the real processes in nature. In reality, if a system is thermally isolated, the temperature of each region of the system is approaching the equilibrium, which is the average temperature of the system. The speed of this process is proportional to the conductance between the region and the surroundings and inversely proportional to the heat capacity of the region. We tried to apply this physical principle, even if it implies that the method cannot be applied to other types of equations.

This method has the following advantages:
1) It is obviously explicit, one can calculate the new values without solving any kind of equation system or even without using matrices. It also implies that the process is easily parallelizable.
2) It is stable for heat conduction type problems, because the new value of the variable T_i is the weighted average of T_i and its neighbours T_j. Indeed, each coefficient in formula (1) is nonnegative and the sum of them is 1. Using this method one can be sure that the solution automatically follows the Maximum and Minimum principles [8], i.e. the extreme values of T occur among the initial values.
3) We state that it is convergent, i.e. if $h \to 0$ then the solution converges to the exact solution. At this moment this statement is based on numerical experiments, but we are working on the rigorous mathematical proof and it is planned to be published in a journal of applied mathematics.
4) It can be easily applied regardless of space dimension, lattice irregularity and inhomogeneity of the heat conduction medium.

We performed numerical tests on several systems, but here we present only 2 different examples.

3. THE FIRST EXAMPLE

The first system is a square-lattice, $N_x = 10$, $N_y = 10$. The capacities are $C_i = 10^{(2-5 \cdot rand)}$; while the conductances are $U_{xi} = 10^{(4 \cdot rand-1)}, U_{yi} = 10^{(4 \cdot rand-1)}$, where *rand* is a random number generated by the MATLAB uniformly in the (0, 1) interval for each block. It means that the capacities (the conductances) follow a log-uniform distribution between 0.001 and 100 (between 0.1 and 1,000). The initial temperatures followed a random function. The task is to solve this system for the temperatures between $t_0 = 0$s and $t_{FIN} = 1$s.

The stiffness ratio (the ratio of the [nonzero] eigenvalues of the matrix with the largest and smallest absolute value) is $6.9 \cdot 10^6$. For the explicit Euler method (which is equivalent to the forward-time central-space FTCS scheme), the maximum possible timestep is

$$h_{\text{MAX}}^{\text{E}} = \left| \frac{2}{\lambda_{\text{m}}} \right| = 3.85 \cdot 10^{-6} s,$$

above this threshold instability necessarily occurs. Here λ_{m} is (non-positive) eigenvalue of the matrix with the largest absolute-value.

In order to check our results, we used the ode45 Runge–Kutta–Dormand–Prince (RKDP) embedded adaptive-stepsize method which is built in MATLAB. First we chose strict error tolerance $\left('RelTol' = 10^{-7}, 'AbsTol' = 10^{-7} \right)$, and with this, our PC needs 9.05 seconds to integrate the equation system. If we start to increase the error tolerance, the running time slowly decreases and can reach 8.37s (while the errors are increasing), but after a threshold, the program fails to converge. Implicit methods developed for stiff systems perform much better: ode23s and ode15s (which uses the Rosenbrock- and the BDF method, respectively, the letter *s* means that these codes were designed especially for stiff systems) solve the task in 0.5s quite precisely. However, as we mentioned before, increasing system size causes major problems for implicit methods, which will be illustrated in the second example.

Now let us try our method without parallelization. If we set the time-step size to h = 0.01, then our computer needs 0.0095s to solve it by our method. The result is presented in *Figure 2*. One can see that we managed to obtain a qualitatively good solution three orders of magnitude faster than the conventional explicit program. If we decrease h to 0.001, the orange line would be almost indistinguishable from the red one, while the running time would be still below 0.1s.
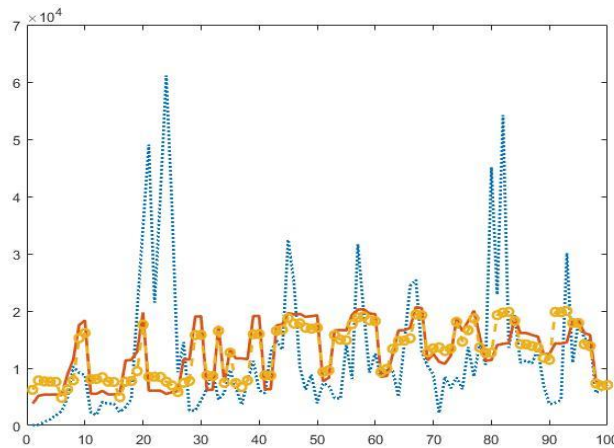
Figure 2. The temperature as a function of the space variable. The blue dotted line represents the initial conditions, the red line is the high-precision solution while the orange circles are the values produced by our algorithm for h = 0.01

A method is said to be *p*th order if the local error is $O\left(h^{p+1}\right)$, or (equivalently for normal systems) if the global error is $O\left(h^p\right)$. On *Figure 3* we present 3 different kinds of the global error. The first one, MaxD is the maximum deviation from the exact (the high-precision) result. The second one, SumD is the sum of the deviations for all of the blocks. The 3rd one, EBE is the energy balance error. It can be calculated without the exact result due to the conservation of energy

$$EBE = \sum_{i=1}^{N} C_i \cdot \left(T_i(t = t_{FIN}) - T_i(t = t_0) \right)$$

One can see that the errors are decreasing slightly faster than the stepsize, thus it can be concluded that the convergence-rate of the method is (at least) one. The right side of the diagram also underpins the statement that the result is stable, as the error does not really increase for increasing stepsize.
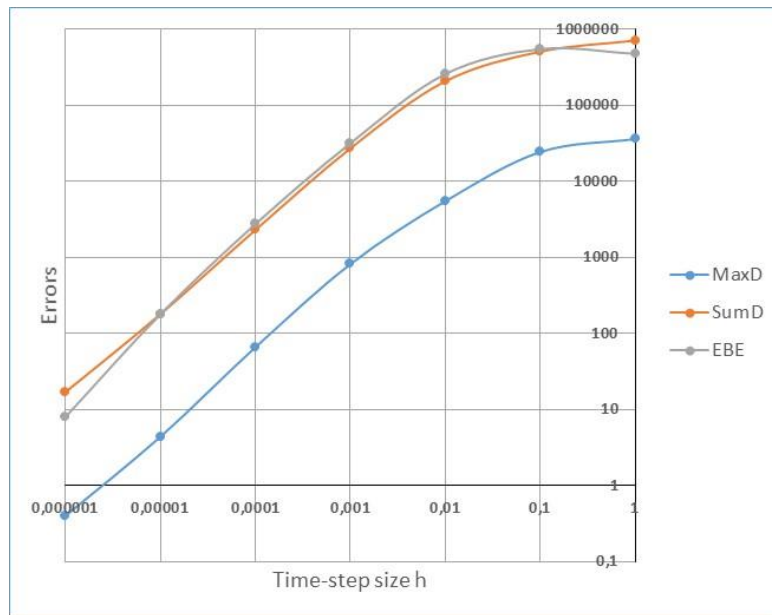
Figure 3. Different kind of errors as the function of the timestep-size.
The blue line is the maximum difference, the orange is the sum of the differences
while the grey one is the absolute value of the energy balance error

4. THE SECOND EXAMPLE

The second system is a rectangle-shaped lattice, $N_x = 400$, $N_y = 10$. The capacities are $C_i = 10^{(3-6 \cdot rand)}$; the distribution of the conductances $U_{xi} = 10^{(6 \cdot rand - 2)}, U_{yi} = 10^{(6 \cdot rand - 4)}$ is anisotropic. The initial temperatures follow a rectangular function:

$$T_\mathrm{i} = \begin{cases} 100 \ \text{if} \ \ 400 \leq i \leq 780 \\ 0 \quad \text{elsewhere} \end{cases}$$

The task is to solve this system for the temperatures between $t_0 = 0\text{s}$ and $t_\mathrm{FIN} = 100\text{s}$. The stiffness ratio of this problem is $1.36 \cdot 10^9$. For explicit Euler method, the maximum possible timestep is $h_\mathrm{MAX}^\mathrm{E} = 1.97 \cdot 10^{-7} s$. Thus explicit methods would require several hours or days to solve this problem, therefore we used implicit BDF method built in ode15s to provide us a reference solution. This MATLAB routine needs 712s to solve the problem with high precision. With loosening the error tolerance we could obtain results in 98s, but not sooner. On the other hand, our method needs roughly 0.0004s for one timestep, thus we can produce a rough but qualitatively good result in a few seconds, which means that we can beat the official routines if the main goal is not the precision but the speed. *Figure 4* reinforces our statement that the method is convergent with at least order 1.
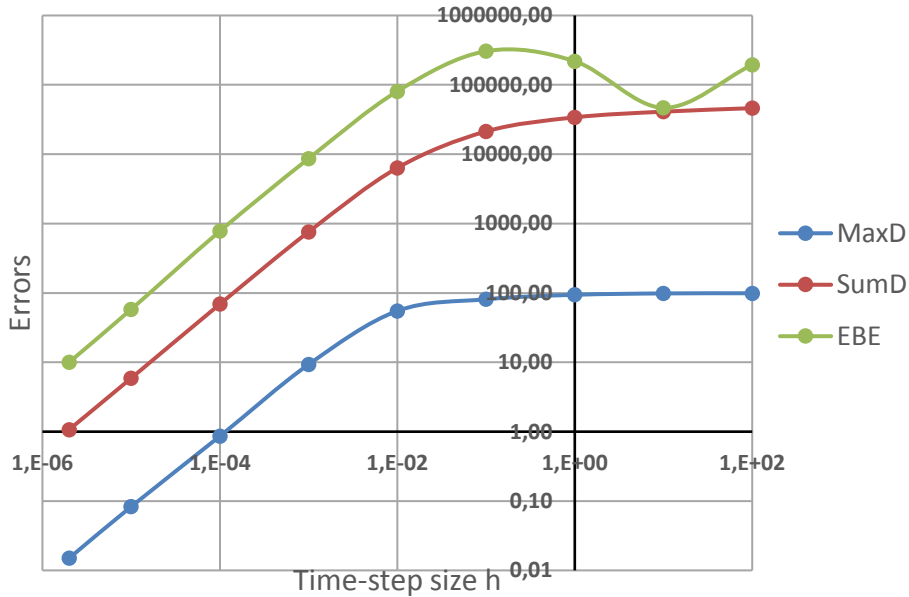
Figure 4. Different kind of errors as the function of the timestep-size.
The blue line is the maximum difference, the orange is the sum of the differences
while the grey one is the absolute value of the energy balance error

One can notice that the absolute value of the energy-balance error increases non-monotonously when the timestep is increased above $h = 1$. In fact, the EBE error changes sign in this region, which calls for caution about the usage of balance-errors as the main basis for error-estimation.

5. SUMMARY

We presented a new numerical algorithm to solve the spatially discretized heat equation without external sources. This method is explicit, stable and convergent. We illustrated the performance of the method in case of two different systems with random parameters. The obtained data suggest that the larger the number of blocks (i.e. the variables in the ODE system) and the stiffness ratio is, the more significant the advantage of our method is, even without parallelization.

However, without fulfilling the following tasks, we could recommend this method only to solve special problems:

- Providing exact mathematical proof of the convergence.
- Working out how to handle source-terms, so that we can tackle problems other than transient problems.
- Elaborating modifications of the method for nonlinear versions of the heat equation, as the parameters like the specific heat usually depend on the temperature as well.
- Develop the adaptive stepsize control version of the method.
- Examine the possibilities for parallel programming of the method.

We are currently working on these projects and the proposed solutions will be published elsewhere.

REFERENCES

[1] Szabó, Sz., Juhász, A. (2003). Messung der Geschwindigkeitsverteilung in großen Strömungsquerschnitten. *VGB PowerTech*, 7/2003, pp. 51–56.

[2] Nabati, H. (2012). Numerical analysis of heat transfer and fluid flow in heat exchangers with emphasis on pin fin technology. *Mälardalen University Press Dissertations*, No. 98.

[3] Baig, H., Antar, M. A. (2008). Conduction / Natural convection analysis of heat transfer across multi-layer building blocks. *5th European Thermal-Sciences Conference*, The Netherlands.

[4] Czibere, T. (1999). *Vezetéses hőátvitel* (Conductive heat transfer). Miskolc: Miskolci Egyetemi Kiadó.

[5] Bencs, P., Bordás, R., Zähringer, K., Szabó, Sz., Thévenin, D. (2010). Application of Schlieren Measurement Technique for Forced Convection from a Heated Circular Cylinder pp. 203–208. In: Stépán, G. T. et al. (eds.). *Gépészet 2010: Proceedings of the Seventh Conference on Mechanical Engineering*. Budapest, Hungary: Budapest University of Technology and Economics, p. 926.

[6] Kovács, E., Majár, J. (2018). On some analogous transient phenomena. *XXXII. microCAD International Multidisciplinary Scientific Conference*, C1/1, Miskolc.

[7] Holmes, M. H. (2007). *Introduction to Numerical Methods in Differential Equations*. Springer, p. 88.

[8] Holmes, M. H. (2007). *Introduction to Numerical Methods in Differential Equations.* Springer, p. 87.

[9] Abdulle, A. (2011). Explicit Stabilized Runge-Kutta Methods. *MATHICSE Technical Report*, Nr. 27.

[10] Özişik, M. N. et al. (2017). *Finite Difference Methods in Heat Transfer*. eBook, CRC Press, p. 224.

[11] M. Hochbruck, M. & Ostermann, A. (2010). Exponential integrators. *Acta Numerica*, 19, pp. 209–286.

HCF DESIGN CURVES FOR HIGH STRENGTH STEEL WELDED JOINTS

HAIDAR MOBARK[1]–JÁNOS LUKÁCS[2]
Institute of Materials Science and Technology,
Faculty of Mechanical Engineering and Informatics, University of Miskolc [1, 2]
H-3515 Miskolc-Egyetemváros
mobark.mechanical@gmail.com[1], janos.lukacs@uni-miskolc.hu[2]

Abstract: The objective of this article is to present the newest results of our complex research work related to the high cycle fatigue (HCF) resistance of advanced high strength structural steels (HSSS). RUUKKI Optim 700QL and SSAB Weldox 700E steels were used for the investigations with 690 MPa yield strength. During the HCF tests base materials and their welded joints using gas metal arc welding as a joining process were tested at different mismatch conditions [matching (M), overmatching (OM), and matching/overmatching (M/OM)] for optimising welding process to achieve an improvement in the fatigue strength. Statistical approach was applied during the preparation and the evaluation of the investigations, which increased their reliability. The parameters of the determinable HCF design curves were calculated based on the philosophy of the Japanese method (JSME S 002-1981). During the investigations and the evaluation the results were compared with each other and with literary data.

Keywords: high strength structural steel (HSSS), RUUKKI Optim 700QL, SSAB Weldox 700E, high cycle fatigue (HCF)

1. INTRODUCTION

Welded joints have been used in the majority of engineering applications such as engineering structures, power generation, offshore structures, and transportation. Welded structures are very sensitive parts because the welded regions are in complex metallurgical and stress conditions. Before the Second World War, the design of all engineering structures was based on tensile strength and ductility. Mild steel was used as the structural material and the minimum yield strength of the weld metal was found to be around 340 MPa. The yield strength to tensile strength ratio of the weld metals that were used for welding the mild steel in early designs was very high and the designers did not pay much attention to the yield strength of the weld metals. It has been reported that the maximum yield strength of the filler metal that has been used for joining the mild steel plates was about 59% higher than the base material [1].

High strength structural steels (HSSS) with yield strengths from 690 MPa upwards are applied in growing amount industrial applications. Specific design solutions and economic aspects of modern steel constructions e.g. mobile cranes or hydro power plants, lead to an increasing trend in light-weight design. Steel producers currently provide a diversified spectrum of high-strength base materials

and filler metals. Thus an extensive reduction in weight and production costs can be achieved with increasing material strength [2].

During the welding process the joining parts are affected by heat and force, which cause inhomogeneous microstructure and mechanical properties, and furthermore stress concentrator places can form. Both the inhomogeneity of the welded joints and the weld defects play important role in case of cyclic loading conditions. High cycle fatigue (HCF) phenomenon is a very common problem in welded structures; however there are a limited knowledge about the fatigue behaviour of HSSS base materials and welded joints up to now. In accordance with the welding challenges nowadays, the mismatch effect was examined. The aim of our present investigations was the determination of basic equations of the HCF design curves for base materials and their differently mismatched welded joints [3].

2. HSSS CLASSIFICATION AND TRENDS OF DEVELOPMENT

For years, metallurgists have been searching ways of producing structural steels which would have the highest (possible) mechanical properties and maintain satisfactory plastic properties at the same time. Due to an increase in yield point, it is now possible to manufacture structures consisting of elements of smaller wall thickness, thus lighter and less expensive to transport. A smaller wall thickness requires a smaller amount of filler metals and a shorter welding time, simultaneously. An increase in the mechanical properties of steels may be obtained by an appropriate selection of chemical composition through a classic process of toughening (hardening and tempering) or by means of thermo-mechanical treatment. However, no matter how high its mechanical properties might be, structural steel will only have practical application if it can be welded by means of commonly used arc methods; toughened steels offer such a possibility. Due to the appropriate selection of chemical composition and proper heat treatment, these steels are characterised by very good mechanical properties as well as good weldability.

The recent development of structural steels has involved on the one hand toughened steels such as S690Q, S890Q and S960Q and on the other hand thermo-mechanically rolled steels of lower mechanical properties but of a higher impact strength (S355M, S460M and S500M) [4].

Steels of 690 MPa yield have become commercial about three decades ago. They were, like today, essentially produced by water quenching and tempering. In the last years thermomechanical rolling followed by accelerated cooling has become an alternative production route [5].

Due to very high mechanical properties, steels of a yield point in excess of 1,100 MPa have found application in the production of high-loaded elements of car lifts, travelling cranes and special bridge structures. The advantages of using steels with high mechanical properties are visible as regards the costs of transport, plastic working, cutting, and welding [4].

By the use of normalizing process, the yield strength is maximized in 460 MPa, thus new methods have been developed since the seventies, when quenched and

tempered (Q&T or Q+T) group appeared. With this heat treatment process, combined with alloying components, the maximal yield strength can reach 1,300 MPa. On the other hand, it should not be ignored that filler metals are not available, up to now, for this extreme strength, only if undermatching (approximately 15–20%) is allowed. It is important to note that applying undermatching during the selection of the filler metal may have some additional positive effects (residual stress, fatigue properties etc.). Due to the above mentioned causes, instead of S1100Q and S1300Q, the S960Q is more widespread, which can be welded by matched electrodes, as well. By the recent development of the thermomechanical (TM) process, the yield strength of TM steels have approached (Q&T) steels, thus it is worth examining this group by the upcoming welding researches [6]. *Figure 1* summarizes the chronology of structural steel developments [7], [8].
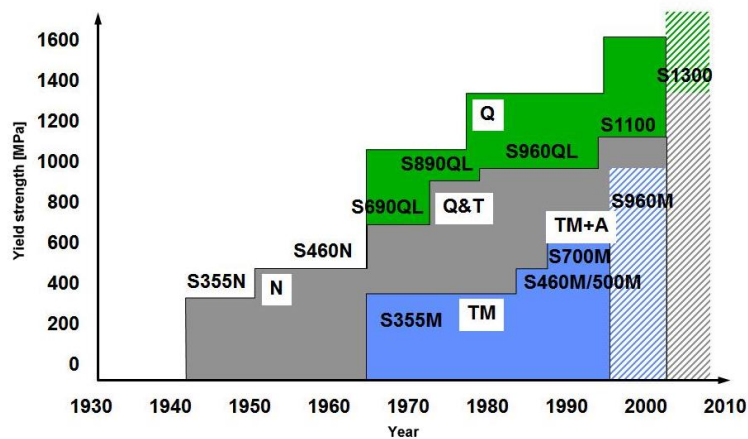
Figure 1. Chronology of structural steels developments [7], [8]

3. PRODUCTION PROCESSES OF TOUGHENED STEELS

The aim of quenching and tempering (Q+T) is to produce a microstructure consisting mainly in tempered martensite. Some amounts of lower bainite are also acceptable. Quenching of high strength steels is performed after austenitizing at temperatures of some 900 °C. In order to suppress during cooling, the formation of softer microstructure, such as ferrite, an accelerated cooling is necessary. The fastest cooling is obtained by exposing the plate surfaces to a rapid water stream. By such an operation the very surface is cooled to temperature below 300 °C within a few seconds. At the core of a plate cooling is essentially slower and the cooling rate decreases with increasing the plate thickness. At the core of thick plates the heat flow to the surface is the controlling parameter for the cooling rate. Closer to the surface and for thinner plates also parameters controlling the heat transfer, e.g. water temperature or flow rate are of importance [5]. The connection between yield strength and transition temperature ranges for different high strength steel types can be seen in *Figure 2* [5], [7], [9].

The development of steel metallurgical processes aims on the one hand the growing of efficiency (reduction of production costs), and on the other hand the decreasing of impurities in steels, which could cause disadvantages, e.g. lamellar tearing or hot cracking [4]. *Table 1* summarizes the characteristic metallurgical periods and the belonging values of the impurities [4].
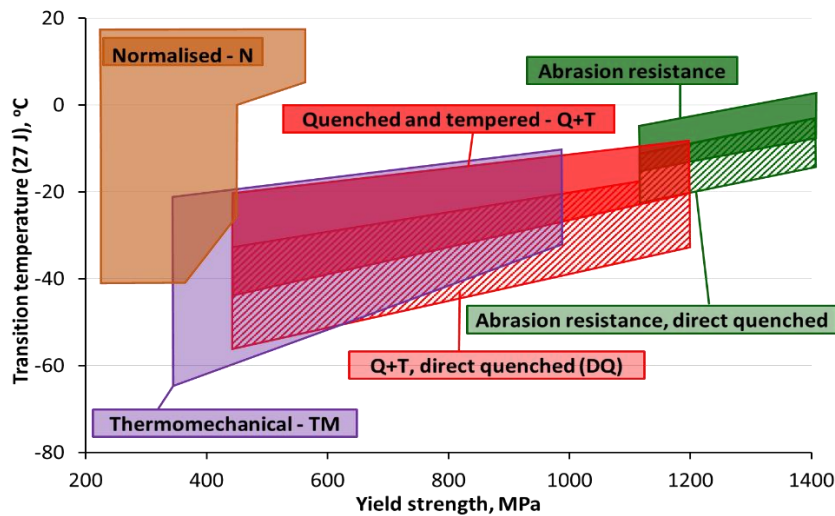
Figure 2. Combination of strength and toughness typical for commercial steels
[5], [7], [9]

Table 1

Impact of development of metallurgical processes on the level of impurities in steel [4]

Element	Metallurgical processes in the years		
	1950/1960	**1980/1990**	**1990/2010[2]**
	ppm		
Sulphur	100–300	50–80	60
Phosphorus	150–300	80–140	6
Hydrogen	4–6	3–5	–
Nitrogen	80–150	<60	–
Oxygen	60–80	<12[1]	–

[1] Technology made it possible to obtain the oxygen content at the amount <12 ppm however in practice, the oxygen content in steel was higher.
[2] The manufacturers do not indicate the content of hydrogen, nitrogen and oxygen.

By applying this methods one can produce steels which have a carbon equivalent lower than approximately 0.05%. Such steels are characterised by better weldability in comparison with steels produced in a conventional way. Schematic diagrams of the production processes of toughened steels are shown in *Figure 3* [4].
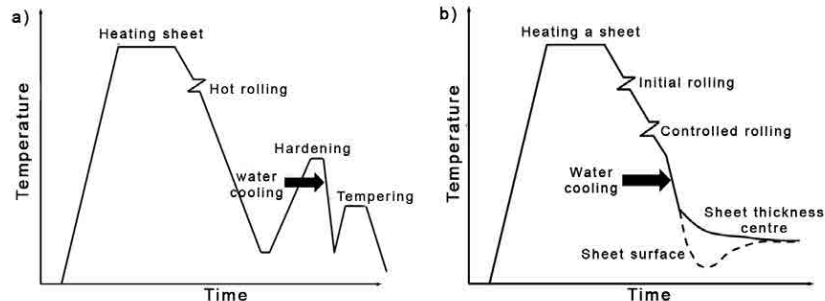
Figure 3. Diagrams of production processes of toughened steels
a) hardening and tempering processes, b) direct hardening process [4]

While developing a technology for welding of toughened steels characterised by high mechanical properties, one should also focused on apart from cold crack formation, such phenomena as follows: welding-induced HAZ softening ("soft layer issue"); failure to obtain a required toughness level in the weld and HAZ (brittleness caused by ageing and precipitation hardening). "Soft layer issue" during welding of toughened steels develops in their HAZ a softened microstructural area with worse mechanical properties. This phenomenon is particularly visible in steels after rolling and intensified cooling. *Figure 4* presents hardness changes in the cross-section of the welded joint made of toughened steel (Q+T). In the HAZ of toughened steel a hardness decrease is to a small extent caused by phase transitions; much greater in this case is the impact of tempering. Welding with limited linear energy makes the layer narrow. In this case, although the hardness of this layer is lower, this fact, due to a narrow softening zone, does not have to result in the deterioration of the mechanical properties of the joint, because of the "contact strengthening" phenomenon generated by plain strains induced in the soft layer [4].
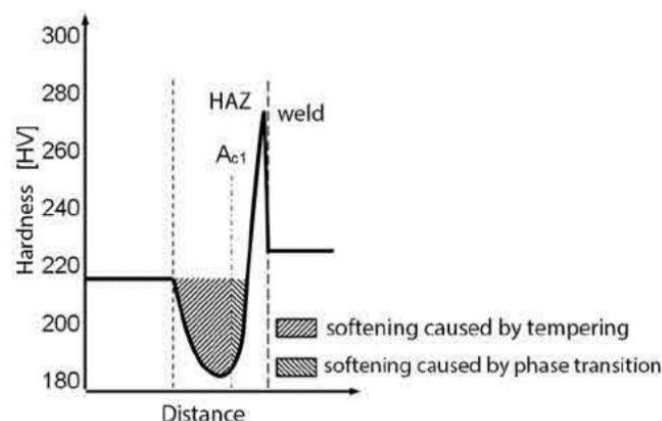
Figure 4. Hardness distribution in welded joint made of toughened steel (Q+T)
where $R_y > 500$ MPa and $t_{8/5} = 30$ s [4]

4. INFLUENCES OF MISMATCHING

The development of high strength low alloy steels, micro-alloyed steels and quenched and tempered steels as well as new fabrication techniques changed the engineers to design the structures on the basis of yield strength and fracture toughness instead of tensile strength. With the increased use of high strength base materials, it is very difficult to produce matching (M) and overmatching (OM) welding consumables because the strength and toughness cannot be increased simultaneously. Sometimes, the yield strength of the weld metal used for joining the plates is lower [undermatched (UM)] or higher (overmatched) than the yield strength of the base material.

Mismatched welded joints are joints in which the yield strength and/or the microstructure of the weld metal will be different from that of the base material and HAZ. The factors, which are responsible for heterogeneities, are welding process, consumables, joint design and weld thermal cycle. Undermatched joints are used in repair welding, welding of bridges, pressure vessels and penstocks, etc. They are used to prevent the cracks in the welds, for example an undermatched cap pass reduces the weld toe cracking from cyclic plastic bending during reeling. Similarly, overmatched joints are used in pipeline girth welds, welded offshore structures, cladding and hardfacing etc., for effectively preventing the weld metal failure by small cracks can be found in the weld metal.

In the base material, HAZ and weld metal combinations, the mismatch constraint is caused by both global mismatch and local mismatch. The global mismatch is defined as the ratio of yield strength of weld metal to that of the base material, whereas the local mis-match is defined as the ratio of yield strength of the weld metal to that of the HAZ. The mechanical factors responsible for producing global strength mismatch of weldments are base material yield strength, weld metal yield strength, base material tensile strength and weld metal tensile strength. The net section yielding occurs when plastic deformation is localized to the defective cross section. The gross section yielding occurs when the applied stress exceeds the material yield strength, i.e. when the yield strength of the weld metal exceeds that of the base material. In general, large defects trend to produce net section yielding, whereas small defects are beneficial for obtaining gross section yielding [1].

5. CIRCUMSTANCES OF INVESTIGATIONS

The investigated base materials, the selected filler metals and the pairing of the base materials and filler metals (mismatch conditions: M, OM and M/OM) for our investigations can be seen in *Table 2*.

Table 2

The base material-filler metal pairing during our experiments

Base material	Filler metal	Mismatch condition
RUUKKI Optim 700QL	INEFIL NiMoCr	matching (M)
SSAB Weldox 700E	Thyssen UNION X85	matching (M)
SSAB Weldox 700E	Thyssen UNION X90	overmatching (OM)
SSAB Weldox 700E	Thyssen UNION X85/UNION X90	matching/overmatching (M/OM)[1]

[1] M/OM = M root layers / OM filler layers

The chemical composition and the basic mechanical properties of the investigated base materials and used filler metals are summarized in *Table 3* and *Table 4*, respectively. Gas metal arc welding (GMAW) was selected for the welding experiments. Based on industrial experiences, M21 mixed gas with 18% CO_2 + 82% Ar content was chosen as shielding gas; in every cases 1.2 mm diameter solid filler wires were used. In the interest of the uniform stress distribution, X joint preparation was designed, with 80° opening angle and with 1.5 mm gap between the two plates. During the welding, the workpieces were rotated regularly.

Table 3

The chemical composition of the base materials and filler metals (weight %)

C	Si	Mn	Cr	Mo	Ni	S	P	Ti	V	Al	Cu
Base material: RUUKKI Optim 700QL											
0.14	0.30	0.96	0.60	0.19	–	0.002	0.009	0.020	0.005	0.05	–
Filler metal: INEFIL NiMoCr											
0.08	0.50	1.60	0.30	0.25	1.50	0.007	0.007	–	0.090	–	0.12
Base material: SSAB Weldox 700E											
0.14	0.30	1.13	0.30	0.17	–	0.001	0.007	0.009	0.010	0.03	–
Filler metal: Thyssen UNION X85											
0.07	0.68	0.61	0.29	0.61	1.73	0.010	0.006	0.080	0.010	0.01	0.06
Filler metal: Thyssen UNION X90											
0.10	0.80	1.80	0.35	0.60	2.30	–	–	–	–	–	–

Table 4

The mechanical properties of the examined base materials and filler metals

Base material and filler metal designation	Yield strength	Tensile strength	Elongation	Charpy V impact energy (–40 °C)
	MPa	MPa	%	J
RUUKKI Optim 700QL	783	826	19	54
INEFIL NiMoCr	≥ 750	≥ 820	≥ 19	≥ 60
SSAB Weldox 700E	791	836	17	165
Thyssen UNION X85	≥ 790	≥ 880	≥ 16	≥ 53
Thyssen UNION X90	≥ 890	≥ 950	≥ 15	≥ 58

The welding parameters were selected based on both theoretical considerations and real industrial applications (summarized in [8] and [10]) and those can be found in *Table 5*. The table shows the welding current (I), the voltage (U) and the welding speed (v_w), also the preheating (T_{pre}) and the interpass (T_{ip}) temperatures, with the calculated linear energy (E_v) and the calculated critical cooling time ($t_{8.5/5}$) values. The parameters of the root layers (1–2) and the filler layers (3–20/8) are shown separately. During the welding, eighteen filler layers (3–20) were used for RUUKKI

Optim 700QL base material, and six filler layers (3–8) were used for SSAB Weldox 700E base material.

Layer	T_{pre}, T_{ip}	I	U	v_w	E_v	$t_{8.5/5}$
	°C	A	V	cm/min	J/mm	s
Root (1–2)	150	130–140	19.0–20.5	20	700–750	7–8
Filler (3–20/8)	180	280–300	28.5–28.5	40	1000–1100	9–11

HCF experiments were performed on base materials and on their welded joints, with an MTS 810 type electro-hydraulic materials testing equipment, at room temperature and in laboratory environment. Flat test specimens and constant load amplitude were applied during the tests, with R = 0.1 stress ratio, f = 30 Hz loading frequency, and sinusoidal loading wave form. The geometry, the location, and the one group of the tested specimens in butt weld joint (BWJ) can be seen in *Figure 5*.
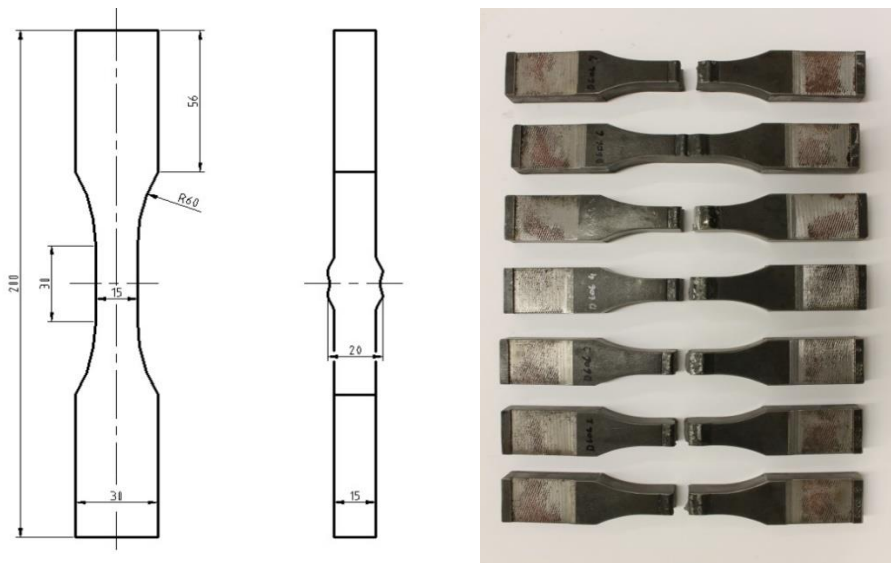
Figure 5. Configuration of the tested specimens (BWJ = butt welded joint)

6. HIGH CYCLE FATIGUE TEST RESULTS

Considering the large number of test specimen and striving after reliability, applying of a statistical approach was necessary. Staircase method was used during both the preparation and the evaluation of the HCF test, based on the JSME S 002-1981 prescription [11]. The results of our experiments were compared with some literature data [12]–[14]. The measured values and the basic lines of the determinable HCF

design limit curves for the base materials (see [15] too) and their welded joints are presented in *Figures 6–7* (literary data) and *Figures 8–9* (own data). In the figures x/y = centre line of the specimen/crack growth direction, h = parallel to the rolling direction, k = perpendicular to the rolling direction, v = thickness direction, 1 W = centre line of the welded joint, 3 W = thickness direction in the welded joint.
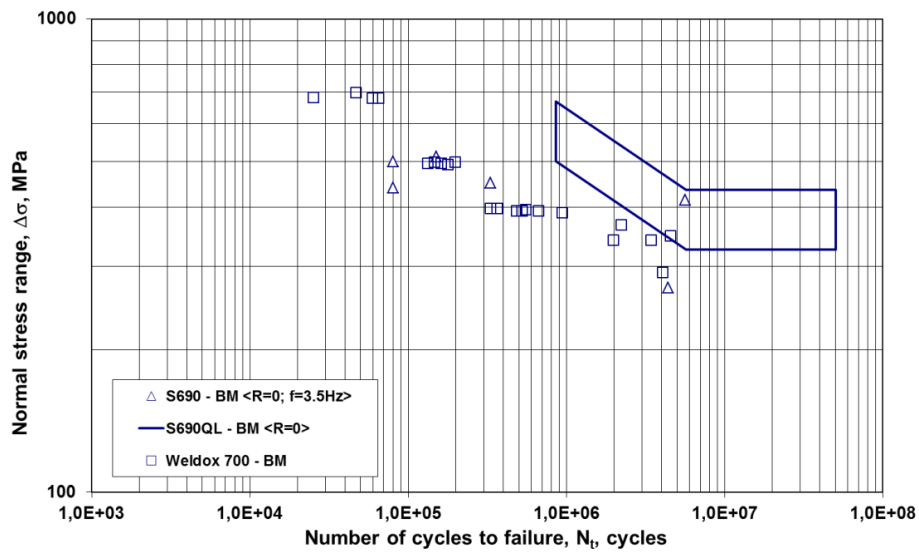
Figure 6. Measured values for S690 type base materials (BM) [12]–[14]
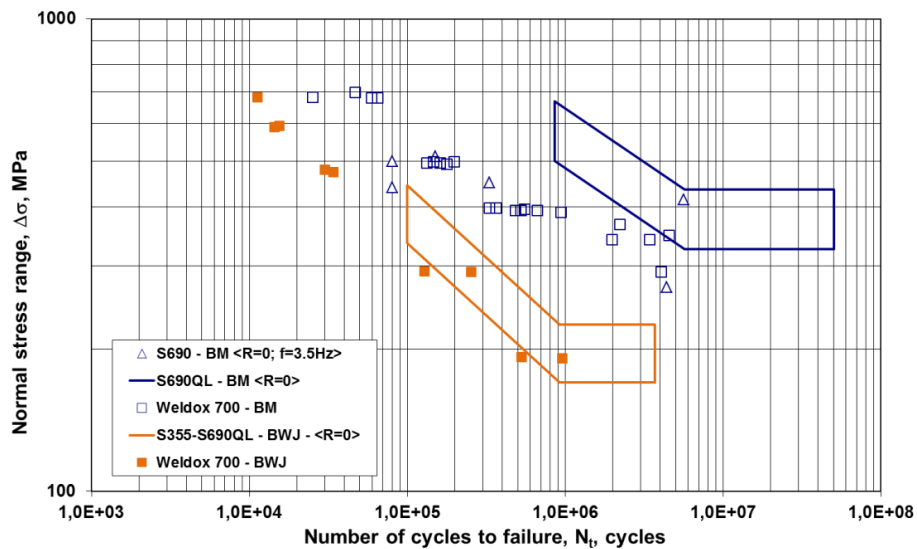
Figure 7. Measured values for S690 type base materials (BM)
and butt welded joints (BWJ) [12]–[14]
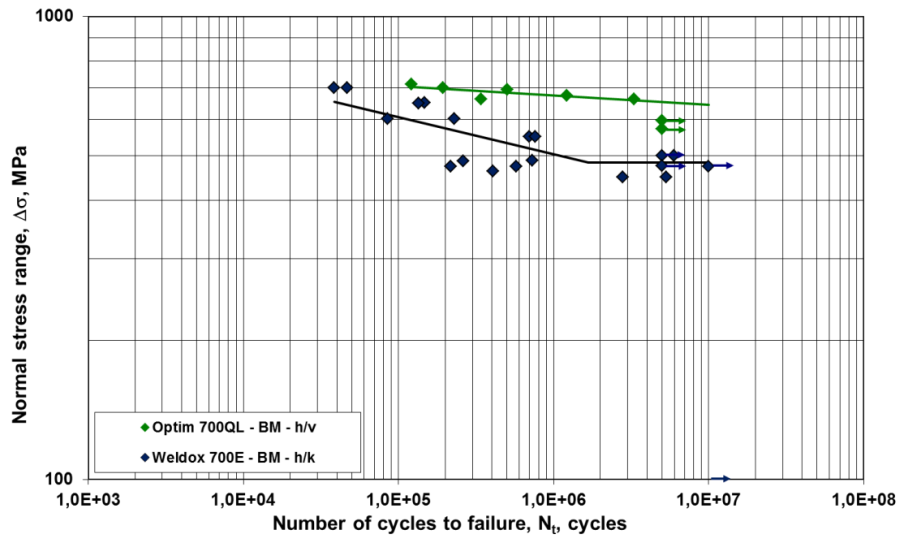
Figure 8. Measured values for S690 type base materials (BM) [own data]
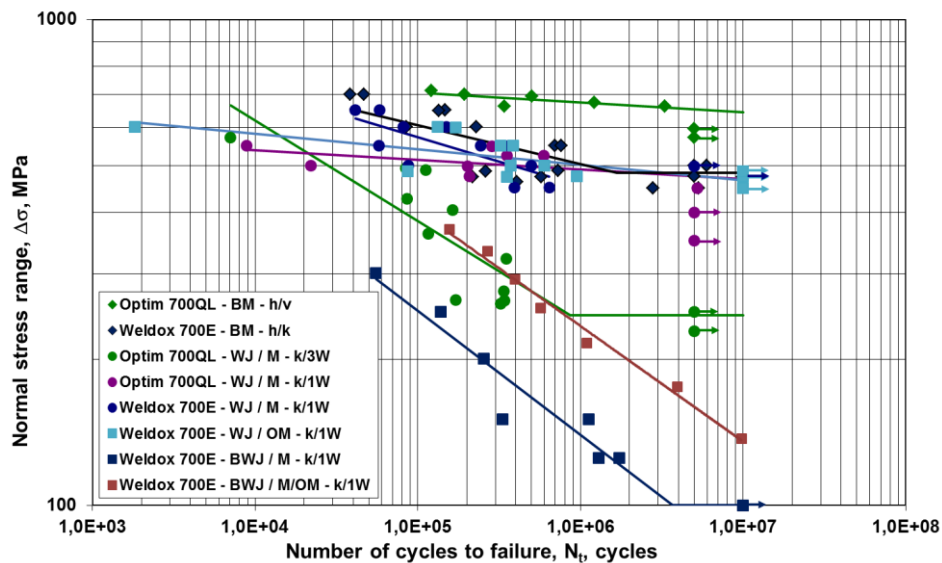
Figure 9. Measured values for S690 type base materials (BM), welded joints (WJ) and butt welded joints (BWJ) [own data]

Table 6 summarizes the basic parameters of the determinable HCF design curves, the N_k value is the number of cycles for the break point of the S-N curve, the $\Delta\sigma_D$ is the fatigue limit, and the $\Delta\sigma_{1E07}$ is the stress value belonging to 1×10^7 cycles in the

cases, when the horizontal (endurance limit) part of the curves cannot be determined. The used equation is as follows:

$$N * \Delta\sigma^m = a,$$

and the HCF design limit curves can be calculated with the help of *–2SD* values.

Basic parameters of the determinable HCF design limit curves

Mismatching and orientation	m	lg(a)	N_k	$\Delta\sigma_D$	$\Delta\sigma_{1E07}$
	–	–	cycle	MPa	MPa
Base material: RUUKKI Optim 700QL					
BM h/v	51.282	151.109	–	–	646
WJ/M k/3W	4.826	17.476	8.639E05	246	–
WJ/M k/1W	50.251	141.260	–	–	470
Base material: SSAB Weldox 700E					
BM h/k	12.453	39.650	1.677E06	483	–
WJ/M k/1W	9.960	32.469	–	–	–
WJ/OM k/1W	31.250	90.415	–	–	467
BWJ M k/1W	3.917	14.400	3.683E06	100	–
BWJ M/OM k/1W	4.207	15.966	–	–	–

7. SUMMARY AND CONCLUSIONS

Based on our investigations and their results the following conclusions can be drawn.

The results of the executed investigations justified the necessity of statistical approaches, especially referring to the directions of the base materials and the welded joints, and the determination of the number of the tested specimens.

Applying the developed welding technologies adequate welded joints can be produced, where the appropriate quality contains the eligible resistance to high cycle fatigue.

The resistance of the base materials to high cycle fatigue is more advantageous than the resistance of the welded joints; the mismatch phenomenon (matching, overmatching and matching/overmatching) has characteristic influence on the high cycle fatigue resistance.

Based on the Basquin equation, calculated curves can be used for the determination of high cycle fatigue design limit curves, applying *–2SD* philosophy

Further examinations required to draw statistically more establish conclusions, to calculate the parameters of the high cycle fatigue design limit curves reliably, to study the effects of the welding residual stress fields, and to determination of design limit curves for different type of whole welded joints.

REFERENCES

[1]   Ravi, S., Balasubramanian, V., Nemat Nasser, S. (2004). Effect of Mis-Match Ratio (MMR) on Fatigue Crack Growth Behaviour of HSLA Steel Welds. *Engineering Failure Analysis*, Volume 11, Issue 3, pp. 413–428, June 2004.

[2]   Schroepfer, D., Kannengiesser, T. (2016). Stress Build-Up in Hsla Steel Welds Due to Material Behavior. *Journal of Materials Processing Technology*, Volume 227, pp. 49–58.

[3]   Mobark, H. F. H., Lukács, J. (2018). Mismatch Effect Influence on the High Cycle Fatigue Resistance of S690QL Type High Strength Steels. *2nd International Conference on Structural Integrity and Durability*, Dubrovnik Croatia, October 2–5.

[4]   St. Weglowski, M. (2012). Modern Toughened Steels – Their Properties and Advantages. *Biuletyn Instytutu Spawalnictwa*, Number 2, pp. 25–36.

[5]   Richter, K., Hanus, F., Wolf, P. (2005). Structural Steels of 690 MPa Yield Strengths – A State of Art. *High Strength Steel for Hydropower Plants Conference*, Graz.

[6]   Gáspár, M., Balogh, A. (2013). GMAW Experiments for Advanced (Q+T) High Strength Steels. *Production Processes and Systems*, Volume 6, Number 1, pp. 9–24.

[7]   Kömi, J. (2011). *Hot-Rolled Ultra-High-Strength Steels of Ruukki*. Trainers' training, Raahe, Finland, June 14, 2011.

[8]   Balogh, A., Dobosy, Á., Frigyik, G., Gáspár, M., Kuzsella, L., Lukács, J., Meilinger, Á., Nagy, Gy., Pósalaky, D., Prém, L., Török, I.; (eds.) Balogh, A., Lukács, J., Török, I. (2015). *Weldability and the properties of welded joints.* (In Hungarian) University of Miskolc, Miskolc, 324 p.

[9]   Laitinen, R. (2011). *Welding of High and Ultra High Strength Steels*. Trainers' training, Raahe, Finland, June 14, 2011.

[10]   Dobosy, Á. (2017). *Design Limit Curves for Cyclic Loaded Structural Elements Made fo High Strength Steels*. PhD Thesis, István Sályi Doctoral School, University of Miskolc, Miskolc (In Hungarian).

[11] Nakazawa, H., Kodama, S. (1987). Statistical S-N testing method with 14 specimens: JSME standard method for determination of S-N curves. In: Tanaka, T., Nishijima, S., Ichikawa, M. (eds.). *Statistical research on fatigue and fracture. Current Japanese materials research*. Volume 2, pp. 59–69. Elsevier Applied Science and The Society of Materials Science, Japan.

[12] Pijper, R. J. M., Kolstein, M. H., Romeij, A., Bijlaard, F. S. K. (2007). Fatigue experiments on very high strength steel base material and transverse butt welds. *Advanced Steel Construction*, Volume 5, Issue 1, pp. 14–32.

[13] Hamme, U., Hauser, J., Kern, A., Schriever, U. (2000). Einsatz hochfester Baustähle im Mobil-kranbau. *Stahlbau*, Volume 69, Issue 4, pp. 295–305.

[14] Stemne, D., Narström, T., Hrnjez, B. (2012). *Welding Handbook. A guide to better welding of Hardox and Weldox*. 1st edition. SSAB Oxelösund AB.

[15] Mobark, H. F. H., Dobosy, Á., Lukács, J. (2018). Mismatch Effect Influence on the HCF Resistance of High Strength Steels and Their GMA Welded Joints. In: Jármai, K., Bolló, B. (eds.). *VAE 2018, Lecture Notes in Mechanical Engineering*. pp. 755–767. Springer International Publishing AG, part of Springer Nature.

DESIGN ASPECTS OF A ROBOTIC END-EFFECTOR

LÁSZLÓ RÓNAI

University of Miskolc, Robert Bosch Department of Mechatronics
3515 Miskolc-Egyetemváros
ronai.laszlo@uni-miskolc.hu

Abstract: Design aspects of a robotic end-effector are discussed in this paper, which is planned to mount onto a Fanuc LRMate 200iC industrial robot. The end-effector is used for sophisticated assembling tasks therefore a load cell is built into the unit. It is a design target that the measured force in the gripper has only axial direction. The rest of the forces and torques are eliminated by two built-in thin plates. Strength analysis of the load cell and the stiffness effect of the plates are calculated and also considered in the assembling force values.

Keywords: *end-effector, FEM, load cell, strength analysis*

1. INTRODUCTION

Due to lack of human resources, nowadays even in Hungary more and more robots are applied in small and middle size companies. Robots are used not only for lading different workpieces but for sophisticated applications, e.g., assembling, welding, machining, etc.

The industry demands such robotics, which are based on haptic concept. The term haptic is originated from Greek, it means 'sense of touch' [1]. The machine haptic could be based on the one hand measurement of the forces, moments in the joints and on the other hand measurement by the end-effector. There is a great variety of commercially available end-effectors, which are used on robots. However special end-effectors often required in special purpose assembling tasks.

An elastic element with strain gauges, i.e., 6 axis force-torque sensor is developed in ref. [2] to create an intelligent end-effector for polishing operations. Naturally there are commercially available end-effectors equipped with force sensors [3] but those cannot be programmed, e.g., complicated industrial operations like snap-fit problems. However in ref. [3] also deals with the opportunity of the human hand guiding. Robotic grippers are also important in agricultural applications, e.g., for fruit harvesting [4].

3D printed fingertips can be useful in many fields like assembling. Ref. [5] contains three main types of 3D printed fingertips: integrated capacitive touch sensing, integrated bend sensors and integrated fingertips with electromechanical switches. Ref. [6] deals with a sensor fusion, which can perform robot force control. The device contains a 6 axis force sensor and an accelerometer.

The main purpose of this paper to design of an intelligent and relatively cheap end-effector, which equipped with a microcontroller (μC) and could be programmed

for sophisticated industrial assembling processes. The unit is planned to contain a load cell to measure the assembling force between ±200 N. Two plates are built in to constrain the deflection of the load cell only in one direction. Therefore the unit can measure the force only in axial direction.

The paper is organized as follows. In Section 2, the schematic of the planned end-effector is discussed. The strength analysis of the elements of the desired end-effector are detailed in Section 3. The FEM simulation of the load cell is performed by Autodesk Inventor 2016 software. The deflection-load curve of the two plates is also determined. The concluding remarks are presented in Section 4.

2. SCHEME OF THE END-EFFECTOR

In this section the design aspects of an end-effector are discussed. This unit consists of a load measurement system equipped with a μC and a traditional pneumatic gripper. The end-effector is planned to mount onto a Fanuc LRMate 200iC industrial robot. The mounting holes of the robot are shown in *Figure 1*, where the diameter of the light grey coloured connecting element is Ø 40 mm.
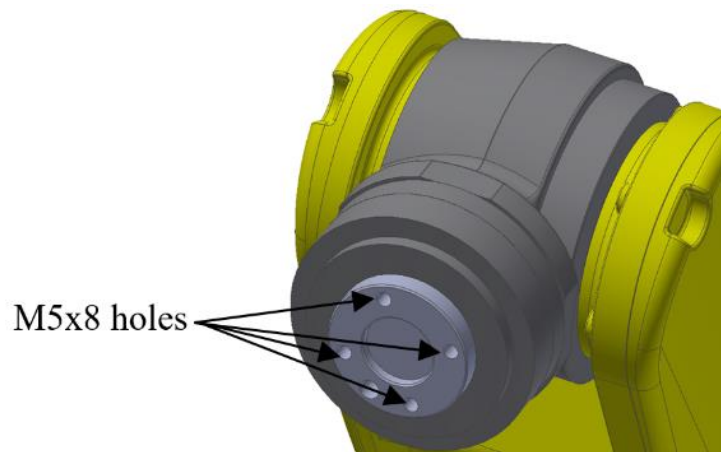
Figure 1. Connecting element of the robot with the mounting holes

The scheme of the end-effector is shown in *Figure 2*. The beam type load cell can measure the assembling force since it has four strain gauges, which are used in a Wheatstone bridge configuration. The load cell purposed to measure shear force in general. To perform accurate force measurement two steel rectangle plates are mounted onto the load cell, which is practically a flexible parallel mechanism. The ends of the plates are mounted onto the wall of the end-effector. Thus the structure will measure only the force in the direction of the assembly. A 24 bit sigma-delta A/D converter is built in the μC unit *(see Figure 2)*.
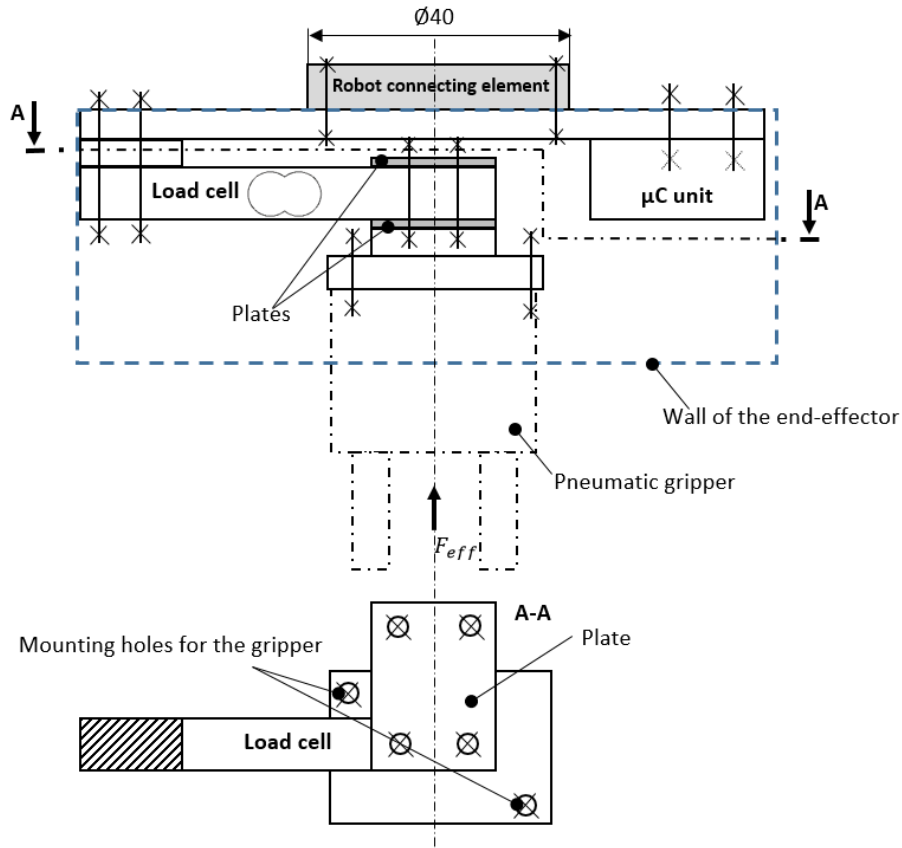
Figure 2. Schematic drawing of the designed end-effector

A Gimatic GS25 type pneumatic parallel gripper will be used to grip work pieces. It can be mounted onto the intelligent end-effector with two M6 × 12 threaded holes. One dowel pin and one centring disc are needed to set the reference position of the gripper. The robot has built-in pneumatic valves therefore the gripper will be actuated from the system program. The maximum closing force of the unit is 127 N at 6 bar pressure.

3. STRENGTH ANALYSIS OF THE STRUCTURAL ELEMENTS

It is worth to analyse numerically the load cell for the nominal load $F = 200\ N$ in order to determine the maximum deflection, which may occur also on the thin plates. It is assumed that both the load cell and the plates are linear elastic.

Finite element analysis has been performed by Inventor 2016 with a very fine mesh with number of nodal points 560,494 and number of elements 379,030. The displacement is constrained in two M5 holes where the load cell is fixed to the end-effector. The force $F = 200\ N$ is applied in the axis of the pneumatic gripper *(*see *Figure 2).*
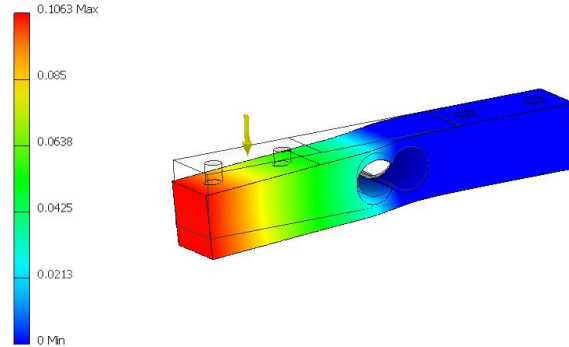
Figure 3. Deflection of the load cell

The deflection of the load cell is shown on *Figure 3* and the distribution of the strain ε_y is displayed on *Figure 4*. The maximum value of the displacement is $0.1063\ mm$. The strain distribution has got four local maximum values in the vicinity of the double cross holes where bending takes place. It should be mentioned that the strains of the opposite strain gauges are equal but with inverse signs. This fact allows the load cell to measure only shear force.

According to *Figure 2* rectangle thin plates are connected to the load cell and to the wall of the end-effector as well. One of the ends of the thin plate is clamped while at the other one the vertical displacement is free but the rotation is constrained as shown in *Figure 5*. In this case the plate is bended only in direction *X*.
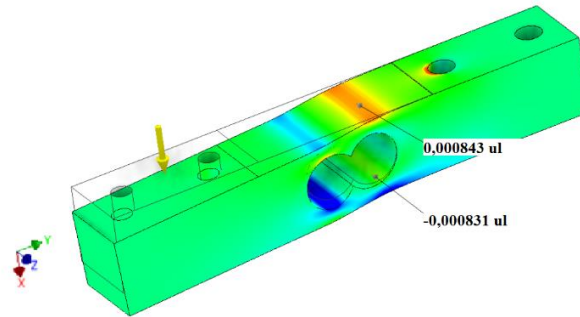
Figure 4. Strain ε_y of the load cell
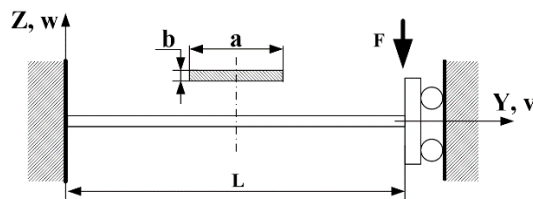
Figure 5. Bending model of the thin plate

This simple plate bending is analogues to a beam bending but it is a plain strain problem therefore the constitution parameters are different. For plate bending the elastic material parameter is calculated as:

$$E_1 = \frac{E}{1 - \nu^2},\tag{1}$$

where E is the Young's modulus, ν is the Poisson's ratio.

<div align="center">

Table 1
Specification of the steel plates

	Value	Dimension
Thickness *(b)*	0.5	[mm]
Wideness *(a)*	23	[mm]
Length *(L)*	21	[mm]
Young's modulus *(E)*	210	[GPa]
Poisson's ratio *(ν)*	0.3	[–]

</div>

The model parameters of the thin plates, i.e., thickness b, width a, length L, Young's modulus E and Poisson's ratio ν are given in *Table 1*.

Since the plate is loaded and constrained only at both ends, thus one beam like finite element is enough to model the problem shown in *Figure 5*. Since there is an analogy between the beam and the single bending plate the stiffness matrix of one plate element can be written as [7], [8]:

$$\boldsymbol{K} = \begin{bmatrix} \dfrac{12IE_1}{L^3} & \dfrac{6IE_1}{L^2} & -\dfrac{12IE_1}{L^3} & \dfrac{6IE_1}{L^2} \\ \dfrac{6IE_1}{L^2} & \dfrac{4IE_1}{L} & -\dfrac{6IE_1}{L^2} & \dfrac{2IE_1}{L} \\ -\dfrac{12IE_1}{L^3} & -\dfrac{6IE_1}{L^2} & \dfrac{12IE_1}{L^3} & -\dfrac{6IE_1}{L^2} \\ \dfrac{6IE_1}{L^2} & \dfrac{2IE_1}{L} & -\dfrac{6IE_1}{L^2} & \dfrac{4IE_1}{L} \end{bmatrix},\tag{2}$$

where L is the length of the plate and I is the area moment of inertia:

$$I = \frac{ab^3}{12}.\tag{3}$$

The equilibrium equation of the plate bending problem for one finite element is written as:

$$\boldsymbol{Kq} = \boldsymbol{f},\tag{4}$$

where $\boldsymbol{f}$ is the column vector containing external force F, $\boldsymbol{q}$ is the vector of generalized nodal displacements

$$\boldsymbol{q}^T = [w_0 \quad \varphi_{x0} \quad w_L \quad \varphi_{xL}]. \tag{5}$$

The displacement boundary condition is given as

$$w(0) = 0, \varphi_x(0) = 0, \varphi_x(L) = 0, \tag{6}$$

it means that there is only one entry, i.e., displacement w_L, which is unknown. Therefore matrix equation (4) is simplified to the following scalar equation:

$$\frac{12IE_1}{L^3} w_L = F \tag{7}$$

Assuming that the displacement w_L is equal to the deflection of the load cell shown in *Figure 2* the supporting force of one plate is

$$F = \frac{12 \cdot 0.2396 \, mm^4 \cdot 230769 \, MPa}{9261 \, mm^3} \, 0.1063 \, mm = 7.6159N. \tag{8}$$

Since two parallel plates are connected to the load cell the effective load producing the maximum displacement will be increased twice of F given in (8), i.e., the force of the two plates is $F_p = 15.2318$ N.
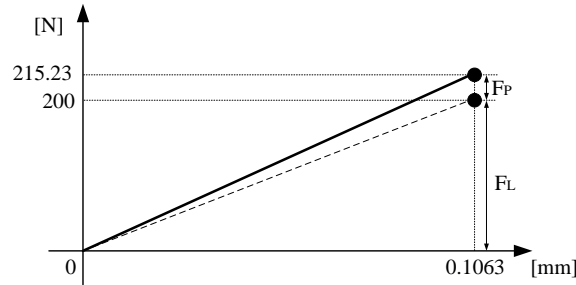
Figure 6. Original and the changed force displacement diagram

The effective load versus deflection diagram of the load measurement structure is shown in *Figure 6*, where the dashed line represents the force arising in the load cell F_L.

If the calibration is performed itself on the load cell then the strain gauges provides only the load cell force, which should be modified with proportional part of F_p in order to obtain the effective load at an arbitrary deflection w_L of the load cell:

$$F_{eff} = w_L \frac{F_L + F_P}{0.1063}. \tag{9}$$

4. SUMMARY

Design aspects of an intelligent end-effector has been discussed in this paper. A cheap beam type load cell, which measures the force has been built into the end-effector. Two thin plates have been connected to the load cell in order to constrain the undesired lateral deflection and axial rotations. This simple but advantageous constructional idea filters out those forces, which are acting not in axial direction.

Simple finite element plate model was used to determine the deflection force of the plates, which is necessary to involve to the determination of the effective axial force. The built-in µC makes it possible to program it for different characteristics of assembly forces, which enables it to handle specific tasks like snap-fit problems.

REFERENCES

[1]	Srinivasan, M. A. (2005). *What is Haptics, The Touch Lab*. MIT.

[2]	Ren, C., Gong, Y., Jia, F., Wang, X. (2016). Theoretical analysis of a six-axis force/torque sensor with overload protection for polishing robot. *23rd M2VIP International Conference, IEEE*, doi: 10.1109/M2VIP.2016.7827338, Nanjing, China.

[3]	Loske, J., Biesenbach, R. (2014). Force-torque sensor integration in industrial robot control. *15th International Workshop on Research and Education in Mechatronics, IEEE,* doi: 10.1109/REM.2014.6920241, El Gouna, Egypt.

[4]	Liu, J., Li, P., Li, Z. (2007). A Multi-Sensory End-Effector for Spherical Fruit Harvesting Robot. *International Conference on Automation and Logistics, IEEE*, doi: 10.1109/ICAL.2007.4338567, pp. 258–262, Jinan, China.

[5]	Zapicu, A., Constantin, G. (2016). Additive Manufacturing Integration of Thermoplastic Conductive Materials in Intelligent Robotic End Effector Systems. *Proceedings in Manufacturing Systems*, Vol. 11, pp. 201–206.

[6]	Grámez García, J., Robertsson, A., Gómez Ortega, J., Johansson, R. (2004). Sensor Fusion of Force and Acceleration for Robot Force Control. *Proceedings of International Conference on Intelligent Robots and Systems*.

[7]	Páczelt, I. (1999). *Végeselem-módszer a mérnöki gyakorlatban.* I. kötet, Miskolc: Miskolci Egyetemi kiadó (in Hungarian).

[8]	Bathe, K. J. (1996). *Finite Element Procedures*. Prentice Hall, Upper Saddle River, New Jersey.

REVIEWING COMMITTEE